Ocean Sci. Discuss., https://doi.org/10.5194/os-2018-49
Manuscript under review for journal Ocean Sci.
Discussion started: 28 June 2018
© Author(s) 2018. CC BY 4.0 License.

Ocean Science
Discussions
Open Access
EGU

Spectral signatures of the tropical Pacific dynamics from model and altimetry: A focus on the meso/submesoscale range

Michel Tchilibou[1], Lionel Gourdeau[1], Rosemary Morrow[1], Guillaume Serazin[1], Bughsin Djath[2], Florent Lyard[1]

1) Laboratoire d'Etude en Géophysique et Océanographie Spatiales (LEGOS), Université de Toulouse, CNES, CNRS, IRD, UPS, Toulouse, France

2) Helmholtz-Zentrum Geesthacht Max-Planck-Straße, Geesthacht, Germany,

Contacts:

Michel tchilibou: michel.tchilibou@legos.obs-mip.fr

Lionel Gourdeau: lionel.gourdeau@legos.obs-mip.fr

Rosemary Morrow: rosemary.morrow@legos.obs-mip.fr

Guillaume Serazin: guillaume.serazin@legos.obs-mip.fr

Bugshin Djath: nathachadjath@gmail.com

Florent Lyard: florent.lyard@legos.obs-mip.fr

Ocean Sci. Discuss., https://doi.org/10.5194/os-2018-49
Manuscript under review for journal Ocean Sci.
Discussion started: 28 June 2018
© Author(s) 2018. CC BY 4.0 License.

Ocean Science
Discussions
Open Access
EGU

Abstract

The processes that contribute to the flat Sea Surface Height (SSH) wavenumber spectral slopes observed in the tropics by satellite altimetry are examined in the tropical Pacific. The tropical dynamics are first investigated with a 1/12° global model. The equatorial region from 10°N – 10°S is dominated by Tropical Instability Waves with a peak of energy at 1000 km wavelength, strong anisotropy, and a cascade of energy from 600 km down to smaller scales. The off-equatorial regions from 10-20° latitude are characterized by a narrower mesoscale range, typical of mid latitudes. In the tropics, the spectral taper window and segment lengths need to be adjusted to include these larger energetic scales. The equatorial and off-equatorial regions of the 1/12° model have surface kinetic energy spectra consistent with quasi-geostrophic turbulence. The balanced component of the dynamics slightly flatten the EKE spectra, but modeled SSH wavenumber spectra maintain a steep slope that does not match the observed altimetric spectra. A second analysis is based on 1/36° high-frequency regional simulations in the western tropical Pacific, with and without explicit tides, where we find a strong signature of internal waves and internal tides that act to increase the smaller-scale SSH spectral energy power and flattening the SSH wavenumber spectra, in agreement with the altimetric spectra. The coherent M2 baroclinic tide is the dominant signal at ~140 km wavelength. At short scales, wavenumber SSH spectra are dominated by incoherent internal tides and internal waves which extend up to 200 km in wavelength. These incoherent internal waves impact on space scales observed by today's alongtrack altimetric SSH, and also on the future SWOT 2D swath observations, raising the question of altimetric observability of the shorter mesoscale structures in the tropics.

Ocean Sci. Discuss., https://doi.org/10.5194/os-2018-49
Manuscript under review for journal Ocean Sci.
Discussion started: 28 June 2018
© Author(s) 2018. CC BY 4.0 License.

1. Introduction

Recent analyses of global sea surface height (SSH) wavenumber spectra from alongtrack altimetric data (Xu and Fu, 2011, 2012; Zhou et al., 2015) have found that while the mid-latitude regions have spectral slopes consistent with quasi-geostrophic (QG) theory or surface quasi-geostrophic (SQG) theory, the tropics were noted as regions with very flat spectral slopes (Fig. 1a). The objective of this paper is to better understand the processes specific to the tropics that contribute to the SSH wavenumber spectral slopes observed by satellite altimetry, particularly in the "mesoscale" range at scales < 600 km, 90 days (Tulloch et al., 2009).

Only a few studies have addressed the tropical dynamics at spatial scales smaller than this 600 km cutoff wavelength. The tropics are characterized by a large latitude-dependent Rossby deformation radius (Ld) varying from 80 km at 15° to 250 km in the equatorial band and theoretically infinity at the equator. Different studies have clearly distinguished the tropical regions dominated by linear planetary waves from the mid-latitudes dominated by non-linear regimes (Fu, 2004; Theiss, 2004; Chelton, 2007). Close to the equator, baroclinic instability is inhibited while barotropic instability becomes more important (Qiu and Chen 2004), and mesoscale structures arise from the baroclinic and barotropic instabilities associated with the vertical and horizontal shears of the upper circulation (Ubelmann and Fu, 2011; Marchesiello et al., 2011). This distinct regime in the tropics raises many questions on the representation of the meso/submesoscale tropical dynamics in the global analyses of alongtrack altimetric wavenumber spectra. How are these complex, f-variable zonal currents folded into alongtrack wavenumber spectra, calculated in 10x10° bins with a dominant meridional sampling in the tropics? Also, the tropics are characterized by strong ageostrophic flow, and the representativeness of SSH to infer the tropical dynamics needs to be checked.

Another dynamical contribution that could flatten the SSH wavenumber spectra in the tropics is associated with high-frequency processes. In altimetric SSH data, the high-frequency barotropic tides are corrected using global barotropic tidal models, and in the tropics away from coasts and islands, these barotropic tide corrections are quite accurate (Stammer et al., 2014). Altimetric data are also corrected for the large-scale rapid barotropic response to high-frequency atmospheric forcing (< 20 days), the so-called Dynamical Atmospheric Correction, using a 2D barotropic model forced by high-frequency winds and atmospheric pressure (Carrere and Lyard, 2003). With only 10 to 35-day repeat sampling, altimetry cannot track the evolution of these rapid barotropic processes, and a correction is applied to prevent aliasing of their energy into lower frequencies. In addition to these large-scale barotropic corrections which are removed from the altimetric data, there exist high-frequency SSH signals from internal tides and internal waves that contribute energy at small scales < 300 km wavelengths. Their impact on SSH wavenumber spectra has been predicted from model analyses in different regions (Richman et al., 2012, Ray and Zaron, 2016), and show that they can dominate in regions of low eddy energy. Dufau et al. (2016) demonstrated that unresolved internal tides can introduce spectral peaks in the altimetric wavenumber spectra from 100-300 km wavelength, and can exceed the level of the internal dynamics especially at low latitudes (Fig. 1b). Recent results from a high-resolution 1/48° model highlight that the tidal and supertidal signals in one region of the equatorial Pacific greatly exceed the internal dynamics at scales less than 300 km wavelength (Savage et al. 2017).

A more technical contribution that can impact on the lower spectral slopes in the tropics concerns

© Author(s) 2018. CC BY 4.0 License.

the altimetric data processing, the spectral calculation and spectral slope estimation. Much attention has been devoted to the effects of altimetric noise (Xu and Fu, 2012; Zhou et al., 2015, Biri et al., 2016) which can flatten the spectral slope calculation if the noise is not removed correctly. Different studies also use different tapering windows to reduce leakage of non-periodic signals in limited-length data series, which can also modify the spectral slope. In global studies, a fixed wavelength band from 70-250 km is often used for the spectral slope calculation (Xu and Fu, 2012; Dufau et al., 2016), which is appropriate for estimating the spectral slope of the energy cascade at mid-latitudes, but may not be well-adapted for the tropics where the maximum spectral slope extends at longer wavelengths, due to the larger Rossby radius there (Fig. 1b).

Thus, the interpretation of altimetric tropical SSH spectra, at spatial scales smaller than 600 km, remains a matter of debate in terms of ocean dynamics. This paper aims at filling this gap by studying the dynamical processes contributing to the small-scale SSH spectra in the tropical Pacific using modeling and observational data. Two different approaches are proposed to better understand the contributions to the observed altimetric flatter spectral slopes. Firstly, we wish to explore the spectral signatures in SSH and EKE of the tropical Pacific mesoscale dynamics (with periods greater than 10 days and wavelengths down to 25 km) and we will concentrate particularly on the tropical "mesoscale" band that varies with latitude. For this, we analyse the global 1/12° DRAKKAR model in the tropical Pacific from 20°S to 20°N, using 5 day outputs covering the period 1987-2001. In comparison to the altimetric analyses of Xu and Fu (2012) or Dufau et al. (2016), this model was specifically chosen to have no high-frequency response to tides, internal waves or rapid tropical waves, and is not limited at low wavelengths by the altimetric instrument noise, but rather by the horizontal grid resolution. We will also use this model to explore the effects of using limited segment lengths or specific windowing when calculating our wavenumber spectra.

In the second part of this paper, we will address the impact on SSH and EKE of the high-frequency components using a unique modelling experiment: we will analyze a higher resolution and high-frequency version of the model: a 1/36° regional model of the south west Pacific (Djath et al., 2014) with and without tides. These two regional model runs have exactly the same configuration and high-frequency atmospheric forcing, both versions include the atmospherically forced internal gravity waves in the tropics. Careful filtering of the barotropic and coherent internal tides from the model with tides also allows us to explore the relative impact of the incoherent tide-ocean circulation interactions, and their signature on the alongtrack wavenumber spectra. This two-model configuration allows us to make a brief investigation of the effects of high-frequency dynamics on the wavenumber spectra, and to discuss the modeled spectra in comparison with altimetric wavenumber spectra based on Topex/Poseidon, Jason and Saral/AltiKa altimeter data. These results will help to better understand the physical content of altimetric observation today, as well as to explore the finer scales that would be captured using future measurements of the SWOT satellite (Fu and Ubelmann, 2014).

In section 2, the different models and data used are presented. In section 3, we discuss processing issues for the spectral calculation, particularly to reduce leakage effects in short tropical segments. In section 4, we discuss the EKE spectral signature of the dynamics over the tropical Pacific as simulated by the 1/12° resolution model. In section 5, results are discussed in term of balanced dynamics and the 1/12° model's SSH spectra are compared to Jason and Saral AltiKa wavenumber spectra. Finally, the contribution of the high-frequency motions to the SSH spectral signature are investigated using

Ocean Sci. Discuss., https://doi.org/10.5194/os-2018-49
Manuscript under review for journal Ocean Sci.
Discussion started: 28 June 2018
© Author(s) 2018. CC BY 4.0 License.

the 1/36° regional resolution model with and without tides, to illustrate its close match with altimetric data. Section 6 presents the conclusions of our study.

2 Models, and altimetric data

2.1 Models

To study mesoscale and submeoscales activity from an OGCM, the model has to properly resolve the corresponding dynamical scales (i.e., be eddy-resolving). The effective resolution for numerical models is that 6-8 grid points are needed to properly resolve dynamical features (Soufflet et al., 2016). In mid latitudes numerical convergence requires ~km horizontal resolution, however in the tropics, because of the larger Ld due the weaker Coriolis force, numerical convergence is obtained from 1/12° horizontal resolution, and the increase of resolution to 1/36° only seems to displace the dissipative range of the model toward smaller scale (Marchesiello et al., 2011). In this paper, we first use a global model at 1/12° resolution, and in a second part we use a regional 1/36° model resolution to investigate the impact of high frequency ageostrophic motions such as baroclinic tides and internal waves.

- Global Model at 1/12°

The model used is the ORCA12.L46-MAL95 configuration of the global 1/12° OGCM developed and operated in the DRAKKAR consortium (www.ifremer.fr/lpo/drakkar) (Lecointre et al, 2011). The numerical code is based on the oceanic component of the NEMO (Nucleus for European Modelling of the Ocean) system (Madec, 2008). The model formulation is based on standard primitive equations. The equations are discretized on the classical isotropic Arakawa C grid using a Mercator projection. Geopotential vertical coordinates are used with 46 levels with a 6m resolution in the upper layers and up to 250 m in the deepest regions (5750 m). The “partial step” approach is used (Adcroft et al., 1997) to allow the bottom cells thickness to be modified to fit the local bathymetry. This approach clearly improves the representation of topography effects (Barnier et al. 2006; Penduff et al. 2007). The bathymetry was built from the GEBCO1 dataset (http://www.gebco.net/data_and_products/gebco) for regions shallower than 200m and from ETOPO2 (www.ngdc.noaa.gov/mgg/global/relief/ETOPO2) for regions deeper than 400m (with a combination of both datasets in the 200m-400m depth range). Lateral boundary conditions for coastal tangential velocity have a strong impact on the stability of boundary currents (Verron and Blayo, 1996). Based on sensitivity experiments, a "partial-slip" condition is chosen, where the coastal vorticity is not set to 0 (“free slip” condition), but is weaker than in the "no-slip" condition. The atmospheric forcing (both mechanical and thermodynamical) is applied to the model using the CORE bulk-formulae approach (Large and Yeager, 2004, 2009).

The simulation started from rest in 1978 with initial conditions for temperature and salinity provided by the 1998 World Ocean Atlas (Levitus, 1998). It was spun up for 11 years using the CORE-II forcing dataset and then integrated from 1989 to 2007 using a 3-hourly ERA-interim forcing (Dee et al., 2011). The 3D velocities, and the 2D Sea Surface Height (SSH) are saved as 5-day means during the period of integration. In the following, it is referenced as G12d5. The domain considered in this study covers the tropical Pacific between 20°N -20°S. This simulation has been used to document

© Author(s) 2018. CC BY 4.0 License.

177 mesoscale variability in the South West Pacific Solomon Sea (Gourdeau et al., 2014; Gourdeau et al.,
178 2017). The present study will analyse this simulation over the tropical Pacific.

179 **- Regional Model at 1/36° with and without tides**

180 As part of the CLIVAR/SPICE program, regional simulations of the Solomon Sea in the South Western
181 tropical Pacific have been performed (Ganachaud et al., 2014). The numerical model of the Solomon
182 Sea used in this study has a 1/36° horizontal resolution, and 75 vertical levels. It is based on the same
183 oceanic component as the NEMO system presented above. This 1/36° resolution model is embedded
184 into the global 1/12° ocean model presented above and one-way controlled using an open boundary
185 strategy (Tréguier et al., 2001). Its horizontal domain is shown on Fig. 3b. The bathymetry of the high-
186 resolution Solomon Sea model is based on the GEBCO08 dataset. Atmospheric boundary conditions,
187 consisting in surface fluxes of momentum, heat and freshwater, are diagnosed through classical bulk
188 formulas (Large and Yeager, 2009). Wind and atmospheric temperature and humidity are provided
189 from the 3-hourly ERA Interim reanalysis (Dee et al., 2011). A first version of the regional model with
190 45 vertical levels has been initialized with the climatological mass field of the World Ocean Atlas
191 (Levitus et al., 1998) and was integrated from 1989 to 2007. More technical details on this
192 configuration may be found in Djath et al. (2014). The new version used here is distinct from the
193 former version by the number of vertical levels (75 levels in the new version) but above all by its
194 ability to take account realistic tidal forcing (Tchilibou et al., 2018). It is of particular importance in
195 this area where internal tides are particularly active (Niwa and Hibiwa, 2011; Gourdeau, 1998), and
196 could modify accordingly the energy flux for the meso and submesoscale bands (Richman et al.,
197 2012). The model is forced at the open boundary by prescribing the first 9 main tidal harmonics (M2,
198 S2, N2, K2, K1, O1, P1, Q1, M4) as defined from the global tides atlas FES2014 (Lyard et al., 2018)
199 through a forced gravity wave radiation condition. The model is initialized by the outputs from the
200 ORCA 1/12° version. Two simulations are performed: one without the tidal forcing (R36) over the
201 1992-2012 period, and one with the tidal forcing (R36T) over the 1992-2009 period. Model outputs
202 are saved as daily mean (R36(T)d), and instantaneous fields are saved hourly (R36(T)h) during a 3
203 month period from January-March 1998.

204 **2.2 Altimetric data**

205 Along-track SSH observations from TOPEX/Poseidon covering a period (January 1993 to December
206 2001) in common with the G12d5 simulations are analyzed over the tropical Pacific domain. The
207 most recent altimetric missions (Jason-2 and SARAL/Altika) are also analyzed over the January-2013
208 to December-2014 period to compare with the signature of the high frequency modelled SSH in
209 R36Th. These data are made available from the Copernicus Marine and Environment Monitoring
210 Service (CMEMS, http://marine.copernicus.eu). TOPEX/Poseidon and Jason-2 are conventional pulse-
211 width limited altimeters operating in the Ku-band (Lambin et al., 2010). SARAL/Altika with its 40 Hz
212 Ka-band emitting frequency, its wider bandwidth, lower orbit, increased Pulse Repetitivity Frequency
213 and reduced antenna beamwidth, provides a smaller footprint and lower noise than the Ku-band
214 altimeters (Verron et al., 2015). For the different missions we will analyze the 1 Hz data, extracted
215 over the same region as our model analysis.

216

217 **3 Spectral methods**

Ocean Sci. Discuss., https://doi.org/10.5194/os-2018-49
Manuscript under review for journal Ocean Sci.
Discussion started: 28 June 2018
© Author(s) 2018. CC BY 4.0 License.

In the following sections we present spectral analyses of the modelled SSH or EKE fields, or the altimetric SSH. The spectral analysis we use is based on Fast Fourier Transforms (FFT) of our signal, which allows us to work with a limited sampled signal. Longer data records enable a better decomposition of the variability at each frequency (wavenumber) and thus a better separation of neighboring frequencies in the spectrum. However, for wavenumber spectra, long spatial data records can mix information from different geographical regimes, especially in the tropics where meridional sections cross the strong zonal currents, making their dynamical interpretation difficult.

Different studies performing spectral analysis of altimetric data or models over the global ocean use very different data length segments to calculate the spectrum. Some altimetric studies use data segment lengths of around 500 km (e.g. Dufau et al., 2016), or 1000 km length tracks averaged in 10° or 20° square box, with or without overlapping (Xu and Fu, 2012). Model spectra (isotropic) are mostly calculated in 10° or 20° square boxes (e.g., Sasaki and Klein, 2012; Biri et al., 2016; Chassignet and Xu, 2017). These data segment lengths may be adequate for the mid-latitudes but are not appropriate for the tropics, when the maximum energy can occur at 600-1000 km wavelengths. Using shorter segments than this reduces the maximum energy and thus the spectral slope. A wide variety of filter windows are applied in the different studies before calculating frequency (wavenumber) spectra to reduce the leakage effect. These include the 10 % cosine taper window or Tukey 0.1 window, referred hereafter as Tk01 (LeTraon et al., 2008; Richman et al., 2012; Dufau et al., 2016); the Hanning window, referred as Han (Capet et al., 2008; Rocha et al., 2016); or making the signal double periodic instead of the tapering, referred as Dbp (Marchesiello et al. 2011; Sasaki and Klein, 2012; Chassignet and Xu, 2017). In the following, we will also consider the Tukey 0.5 window (Tk05).

We tested the sensitivity of our G12d5 model's SSH wavenumber spectrum to the different tapering windows and the double periodic method, using different data length sizes, and in one or two dimensions. The following steps were performed for these test spectra, evaluated within 10°S-10°N/160°W-120°W: the model data are extracted meridionally and zonally in fixed segment lengths of 5°, 10°, 20° and within a 20°X20° square box; the mean and linear trend (fitted plane for two-dimensional case) were removed from each data segment or box; the filter window (Tk01, Tk05, Han) or Dbp are applied ; temporal and spatial (longitude, latitude) series spectra are calculated and averaged in Fourier space. The results are shown in Fig. 2.

Tk01 meridional spectra in the tropics are the most perturbed by the short segment lengths (Fig. 2a). In the 70-250 km range commonly used to define a global mesocale band (delimited by the green vertical lines), the spectral slope flattens as the data segment length decreases. 5° segment spectra with a Tk01 window have a $k^{-1.3}$ slope, which explains the very shallow slope in the tropics observed by Dufau et al. 2016 who applied this short data segment size and a Tk01 window. Meridional spectra differ primarily at larger scales from 100-500 km, when short segment lengths are used (Fig. 2a). A comparison of the meridional spectrum using 20° segments and different windows (Tk01, Tk05, Han and Dbp) are shown in Figure 2b. Even with the 20° segments, Tk01 is distorted. On the other hand, the Tk05, Han and Dbp match well, with a near linear cascade of energy over the 30-1000 km wavelength range, and are more adapted for the tropics since they capture the main range of SSH mesoscale dynamics, particularly the spectral energy peaks around 1000 km wavelength.

Ocean Sci. Discuss., https://doi.org/10.5194/os-2018-49
Manuscript under review for journal Ocean Sci.
Discussion started: 28 June 2018
© Author(s) 2018. CC BY 4.0 License.

Similar calculations were performed for the zonal spectra (not shown) and confirm that the Tk01 method deforms the zonal spectra and flattens the spectral slope within the 70-250 km wavelength band as the data segment size decreases. Tk05, Han and Dbp 20° segment spectra match, although the Dbp has more noise at small scale.

We also conducted a sensitivity test in the off-equatorial region (not shown): Flattening and deformation of the spectrum by Tk01 persist, but the 10° segments or 10° square box are long enough to capture the off-equatorial dynamics.

The particular sensitivity in the tropics to the spectral segment length and windowing is linked to energetic EKE and SSH signals extending out to longer wavelengths. The discrepancies between the different window filters used result from the way they modify the original data. Tk01 preserves more of the long wavelength signal in the original data. However it creates unrealistic variability at shorter wavelengths because of its abrupt transition to zero at the edge of segments. This effect is amplified for short data segments, resulting in more important variability at small scale (for wavelengths near 10 % of the data size). Thus there is more spurious energy near 55 km wavelength for the Tk01 with 5 degree (550 km) segments, near 110 km for the 10° segments, and near 220 km for the 20° segments (Fig. 2a). The Tk01 abrupt transition to zero combines with the low wavenumber leakage and distorts the spectra. There is a minor difference between Tk05 and Han, depending on data variability. The advantage of Tk05 is in retrieving the large-scale peaks which are smoothed with the Hanning filter window. Tk05 is a good compromise for preserving much of the original signal and reducing leakage, but needs to be applied over larger segments. The Dbp technique compares well to Tk05 and Han for one-dimensional spectra. The only problem with this method is the difference at the large-scale and unfiltered spectral fluctuations at small scale.

We conclude that the Tk05 or Hanning filters give similar results in the equatorial band, with a minimum of 15° to 20° needed in segment lengths. We do not advise to use the tk01 filter window, and we choose to use the Tukey 0.5 filter in the paper. In the off-equator region, 10° data segments or 10°X10° boxes are sufficient.

4 Spectral representation of the tropical dynamics

In this section we analyze the spectral signatures of the tropical dynamics by first considering the surface velocity fields of the G12d5 simulation over the open Pacific Ocean. Modeling studies mainly analyze velocity or EKE fields, and we start our spectral analysis by checking that the model represents well the main dynamical processes in the tropics. Surface velocity fields were averaged over the first 40 m depth and include geostrophic and ageostrophic components. The model resolves a domain of variability with periods greater than 10 days, and wavelengths exceeding 25 km, but model dissipation may be active up to 70 km wavelength. Note that the resonant response to the wind forcing through the 3-5 day period, large-scale equatorially trapped inertia-gravity waves, are not represented in G12d5 because of the 5-day averaged model outputs.

The Tropical Pacific is characterized by a series of strong alternate zonal currents and a large range of ocean variability, in response to the atmospheric forcing and to the intrinsic instability of the current system. The main zonal currents spanning the tropical Pacific are shown in Fig. 3: North of 10°N is the westward North Equatorial Current (NEC) and at its northern edge are the eastward SubTropical

© Author(s) 2018. CC BY 4.0 License.

CounterCurrent (STCC) and the Hawaiian Lee CounterCurrent (HLCC) (Kobashi and Kawamura, 2002; Sasaki and Nonaka, 2006); between 3°-8°N is the eastward North Equatorial CounterCurrent (NECC); South of 3°N, the westward South Equatorial Current (SEC) straddling the equator is divided in two branches by the eastward Equatorial UnderCurrent (EUC) that reaches the surface to the east. The eastward South Equatorial Counter Current (SECC) in the south western Pacific is between 6°-11°S. Instabilities of these zonal currents result in meso and submesoscale activity illustrated by a snapshot of vorticity (Fig. 3) that illustrates the description of vortices in Ubelmann and Fu (2011). It is characterized by structures with a large range of scale and strong anisotropy in the equatorial band. The largest structures (~500 km) correspond to the nonlinear Tropical Instability Vortices (TIVs), also associated with the Tropical Instability Waves (TIWs), and occur north of the equator (Kennan and Flament, 2000; Lyman et al., 2007). The off-equatorial regions (10-20° latitude) are characterized by smaller-scale turbulent structures in Fig. 3.

In order to investigate how these well-known tropical dynamics project into frequency or wavenumber spectra, we will analyze separately the equatorial band (10S-10°N) and the off-equatorial band (10°N-20°N and 10°S-20°S) defined by the different boxes in Fig. 3. In the following, the model's representation of the following diagnostics will be discussed together for the each zonal band : the EKE frequency spectra as a function of latitude and longitude (Fig. 4), the zonal EKE wavenumber-frequency (k-ω) spectra and meridional EKE wavenumber-frequency (l-ω) spectra (Fig. 5), and the 1D (zonal/meridional) EKE wavenumber spectra (Fig. 6).

4.1 Equatorial region

The temporal variability of the tropical EKE signal is shown by EKE frequency spectra as a function of latitude and longitude in Fig. 4. In the equatorial band, most of the energy is concentrated within 5° of the equator (Fig. 4a). The highest EKE occurs in this band at annual to interannual scales, but there is still significant energy over all frequencies greater than the 10-days resolved by this model. EKE spectra averaged in latitude over 20°N-20°S are highly influenced by the energetic equatorial dynamics (Fig. 4b). This band includes the equatorial wave guide where waves tend to propagate zonally and are organized into a set of discrete meridional modes (Farrar, 2008). Since zonal wavenumber-frequency spectra are averaged from a number of latitudes within the equatorial band, contributions from the different modes may be seen at once (Fig. 5b). The eastward phase speed (positive wavenumber), due to fast moving Kelvin waves at the equator is visible even if the strong westward propagation (negative wavenumber) just off the equator overpowers the eastward propagation on the equator in the averaged spectrum. We have superimposed on the zonal wavenumber-frequency spectrum the theoretical dispersion curves of the first baroclinic-Rossby waves in a resting ocean. Values of wavenumber and frequency for which the EKE power spectrum is significantly above the background follow relatively well the variance-weighted mean location of dispersion curves for long equatorial waves. Meridional wavenumber-frequency (l-ω) EKE spectra were computed over the 20°N to 20°S section, in different longitude bands spanning the Pacific Ocean. Fig.5d shows an example for the particularly energetic 120°W-150°W band. Other longitude bands across the Pacific show similar spectral energy patterns, but with lower energy levels. Figures 5b,d illustrate the strong anisotropy between the zonal (k,ω) and meridional (l,ω) spectra. The meridional structure of the dominant zonal equatorial waves is well known, with meridional amplitude decaying away from the equator over +/-5° or 550 km. This contributes in the meridional-

Ocean Sci. Discuss., https://doi.org/10.5194/os-2018-49
Manuscript under review for journal Ocean Sci.
Discussion started: 28 June 2018
© Author(s) 2018. CC BY 4.0 License.

345 frequency EKE spectrum to the fairly constant decrease in spectral energy from long wavelengths
346 down to 100-250 km wavelength, in both north and south directions (Fig.5d).
347
348 The ridge of westward variance (Fig. 5b) is nearly vertical, with variance mainly restricted to large
349 wavelengths but also extending to high frequencies in relation with TIW activity. In accordance with
350 observations (Willet, 2006), the modeled TIWs are defined by periods and zonal wavelengths in the
351 range of 15-40 days and 800-2000 km, respectively, and have a meridional propagation with
352 northward and southward motion roughly balanced (Fig. 5d). The 33-day TIW variability is triggered
353 by baroclinic instability of the SEC-NECC system, located between 3°N-5°N and 160°W-120°W (Fig.
354 4a,b). They have an asymmetric structure across the equator with larger energy north of the equator
355 than south of it in accordance with the analysis of TOPEX/Poseidon sea level data by Farrar (2008).
356 The 20-25 days variability, associated with another type of TIW triggers by barotropic instability of
357 the EUC-SEC system (Masina et al., 1999), is centered at the equator, east of 140°W (Fig. 4a,b).
358 Centered at the equator, from the background there is a 60-80 days variability extending from 150°E
359 to 130°W (Fig. 4a,b) associated with intraseasonal Kelvin waves (Cravatte et al., 2003; Kessler et al.,
360 1995) as confirmed by eastward variance and energy centered at l=0 in the zonal and meridional-
361 frequency spectra, respectively (Fig. 5b,d).
362
363 The model represents these tropical signals well, and for wavelengths larger than 600 km the
364 equatorial waves are the dominant signal (Tulloch et al., 2009). For wavelengths smaller than 600
365 km, the variance no longer follows the Rossby wave dispersion curves, and exhibits a red noise
366 character in wavelength, and a nearly white noise in frequency. These rapid motions with 250-600
367 km wavelengths occur in response to wind forcing, wave interactions or current instability. The
368 corresponding zonal EKE wavenumber spectrum (Fig. 6) has a steep slope that continues rising to
369 long wavelengths with a k^{-3} relation reaching a peak at 1000 km, reflecting the zonal scales of the
370 TIWs, before flattening to a k^{-1} power law at larger scale. Below 70 km, EKE spectra drastically
371 steepen as an effect of model dissipation.

372 **4.2 Off equatorial regions**

373 Poleward of 10° the equatorial trapped waves become insignificant, and most of the energy is
374 concentrated at periods greater than 60 days (Fig. 4a). This corresponds with results by Fu (2004)
375 showing a decreasing frequency range with latitude, where the maximum frequency at each latitude
376 corresponds to the critical frequency of the first–mode baroclinic waves that varies from 60 days at
377 10°S to 110 days at 20°S (Lin et al., 2008). The zonal wavenumber-frequency spectrum strongly
378 differs from those in the equatorial belt (Fig. 5a,c), and is closer to the mid latitude spectra (Wunsch,
379 2010; Wakata, 2007; Fu, 2004) with smaller energy in the south tropics than in the north as also
380 reported by Fu (2004). The theoretical dispersion curves for mid latitude first baroclinic Rossby waves
381 are shown for the case of meridional wavenumbers corresponding to infinite wavelengths. At low
382 wavenumbers (i.e., long wavelengths > 600 km) the motions follow the baroclinic dispersion curves.

383 Although linear Rossby wave theory provides a first - order description of the EKE spectra, in both
384 hemispheres energy extends to higher frequencies (Fig. 4a), and as the wavenumber and frequency
385 increases, significant deviations from the baroclinic dispersion curves occur (Fig. 5a,c). Barotropic and
386 baroclinic instabilities, and nonlinear processes might generate energy at periods down to 20-30
387 days, prohibited by the linear dispersion relation (Hughes and Williams, 2010). Much of the energy

Ocean Sci. Discuss., https://doi.org/10.5194/os-2018-49
Manuscript under review for journal Ocean Sci.
Discussion started: 28 June 2018
© Author(s) 2018. CC BY 4.0 License.

lies approximately along a straight line called the 'non dispersive line' in wavenumber–frequency space as it implies non-dispersive motions. The wavenumber dependencies along the 'non dispersive line' could be the signature of non-linear eddies. In fact, for eddies that retain their shapes as they propagate, the energy at every wavenumber must propagate non-dispersively (Rhines, 1975). The westward propagation speed is estimated at ≈ 10 cm/s, close to the eddy propagation speed found in this latitudinal range by Fu (2009) and Chelton et al. (2007). But these regions are defined as a weakly nonlinear regime (Klocker and Abernathey, 2014), and the non-dispersive line may account both for coherent vortices and jet meanders propagating westward at an approximately uniform speed (Morten et al., 2017). So our frequency-wavenumber spectra are consistent both with linear dynamics at low wavenumbers but also with westward-propagating eddy-like coherent vortex structures or jet meanders at higher wavenumbers.

The zonal EKE wavenumber spectra (Fig. 6) in the off equatorial regions exhibit a standard shape with a long-wavelength plateau and a spectral break at about 300-400 km, following by a drop in energy close to a k^{-2}/k^{-3} relation (Stammer, 1997). These steep spectral slopes correspond with an inertial range characteristic of mesoscale turbulence (Xu and Fu, 2011). These different spectra confirm that the northern tropics are more energetic than the southern part with a mesoscale range extending to larger scale. It quantifies the more active turbulence in the northern hemisphere, as illustrated in Fig.3b.

4.3 Anisotropic EKE spectra

Classically, wavenumber spectra are investigated throughout an oceanic basin by dividing the basin in square boxes where spectra are calculated to take account of the regional diversity of QG turbulence properties (Xu and Fu, 2011; Sasaki and Klein, 2012; Biri et al., 2016; Dufau et al., 2016). Here, the spectra analysis of the equatorial and off-equatorial bands described above is revisited in 10°x10° boxes for the off-equatorial region, and in 20°x20° boxes for the equatorial region that are suited to recover the shape of the mesoscale range in the tropics (e.g. section 3). Within each equatorial or off equatorial latitude band, spectra in the different boxes are similar (not shown). Therefore spectra are averaged over all the boxes and we present one mean spectrum representative of the square boxes for each equatorial, and off equatorial bands. In geostrophic turbulence, which is nondivergent to leading-order, isotropy implies that 1D (zonal/meridional) and 2D isotropic wavenumber spectra are identical and follow the same power law. In the tropics there is a stronger anisotropic component of the dynamics, which will be explored in Fig.7.

When we concentrate on the 20°x20° equatorial box, we are limited to scales smaller than 2000 km, and here the meridional EKE spectrum has a higher level of energy than the zonal one (Fig. 7b). It reveals the energetic meridional perturbations due to instabilities of the larger-scale zonal currents. The isotropic EKE spectrum is mostly representative of the meridional one. Note that since alongtrack altimetry is mainly orientated in the meridional direction in the tropics, altimetric SSH measurements are particularly well suited to account for the dominant meridional variability, within the limit of the geostrophic hypothesis. Despite the anisotropy at every scale, the different EKE spectral components have a similar shape, with a continuous k^{-3} slope between 100 and 600 km wavelength. The peak of the EKE spectra corresponds to a wavelength of 1000 km. These modeling results compare relatively well with the analysis of the submesoscale dynamics associated with the TIWs by Marchesiello et al. (2011). They observe a peak of energy around 1000 km corresponding to

Ocean Sci. Discuss., https://doi.org/10.5194/os-2018-49
Manuscript under review for journal Ocean Sci.
Discussion started: 28 June 2018
© Author(s) 2018. CC BY 4.0 License.

the TIW wavelength, and a linearly decay of the spectrum with a slope shallower than -3. It is doubtful to define an inertial band in the equatorial region, but we can say that at wavelengths from 100-600 km, the EKE spectral slope of k^{-3} is consistent with a QG cascade of turbulence.

In the 10°x10° off-equatorial boxes, the energy at long wavelengths is greatly reduced compared to the equatorial band. Yet the zonal, meridional and isotropic EKE spectra are similar for wavelengths up to 250 km (Fig. 7a,c). Their slopes are steeper than k^{-2} at scales smaller than 250 km. So, poleward of 10° the hypothesis of isotropy seems to be relevant for scales up to 250 km even if the flow is supposed to be weakly nonlinear (Klocker and Abernathey, 2014). The peak of the EKE spectra corresponds to a wavelength of 300 km. The EKE slope over the redefined mesoscale range from 100 to 250 km is between -2 and -3 which lies between the prediction of SQG and QG turbulence.

Our modeled zonal frequency-wavenumber spectra differ strongly across the equatorial and off equatorial regions, but show a good representation of the tropical wave and TIW/TIV dynamics. The slope of the ridge of westward variance in the zonal k-ω spectrum in Fig. 5 increases towards the equator. As the slope becomes steeper, more power is concentrated at lower wavenumbers. The change in slope of the ridge itself is related to the change in deformation radius and wave propagation speed (Wortham and Wunsch, 2014). The equatorial region differs from the off equatorial regions in having strong anisotropy with mainly zonally oriented structures (Fig. 7), higher energy at long wavelength due to the strong activity of long equatorial waves, and an overlap between geostrophic turbulence and Rossby wave time scales that produces long waves and slows down the energy cascade to eddies with scales consistent in the tropics with a generalized Rhines scale (Lr) (Theiss, 2004, Tulloch et al., 2009; Klocker et al., 2016; Eden, 2007).

Although geostrophy is not valid at the equator, it is valid poleward from 2° latitude, and since our equatorial wavenumber spectral calculations are averaged or span over 20° in latitude, they include a strong geostrophic component. Even so, the validity of geostrophic turbulence theory is questionable in the equatorial band. Rather, our modeled spectral analysis shows the contrasts between the equatorial and off-equatorial regions for the wavenumber range where a steep slope is observed. In the weakly nonlinear regime of the off-equatorial regions, we find spectral slopes of k^{-2} / k^{-3} over a short 100-250 km wavenumber range. The highly anisotropic, ageostrophic equatorial dynamics are characterized by a peak of energy at 1000 km due to TIWs, and a large “mesoscale” range over 100-600 km wavelength with a k^{-3} spectral slope.

5 Modeled and altimetric SSH wavenumber spectra

5.1 Contribution from low-frequency dynamics

Altimetric SSH only provides access to the balanced, geostrophic component of the surface flow (in addition to signals from the high-frequency internal waves and tides, not included in the G12d5 version of the model used here). Since the tropical regions have a strong ageostrophic component of the flow, we consider how the wavenumber spectra of geostrophic currents (EKEg) differ from that of the total currents analyzed in section 4. Close to the equator, as f approaches zero, the geostrophic current component can still be calculated using the beta approximation, following Picaut et al. (1989). Fig.7 shows the difference between the wavenumber spectra calculated from the total

Ocean Sci. Discuss., https://doi.org/10.5194/os-2018-49
Manuscript under review for journal Ocean Sci.
Discussion started: 28 June 2018
© Author(s) 2018. CC BY 4.0 License.

EKE averaged over the upper 40 m, and from the geostrophic component of EKE estimated at the surface.

In the equatorial band at scales from 300 to 1000 km, the ageostrophic EKE is more energetic, with a stronger contribution to the total EKE than the geostrophic component (Fig. 7b). In the off-equatorial bands (Fig 7a,c), the geostrophic and total EKE spectra are similar at larger wavelengths. However, in all regions, the total EKE is weaker than the geostrophic EKE at scales from 250 km down to the 20 km resolved by the model. Klein et al. (2008) also noted stronger geostrophic EKE at small wavelengths (and weaker spectral slopes) compared to upper ocean EKE spectra in mid latitude regions which had QG slope characteristics. In terms of spectral slope in the equatorial region, using the geostrophic EKE rather than the total EKE tends to flatten the spectra in the 600-110 km mesoscale range, and changes the spectral slope from k^{-3} to k^{-2}. In the off-equatorial regions, the geostrophic EKE has a slightly flatter spectral slope between -2 and -3 in the 100-250 km band.

Since the altimetric groundtracks have a more meridional orientation in the tropics, the altimetric SSH spectra should be like the model's meridional SSH spectra that are shown on Figure 8. SSH meridional wavenumber spectra (Fig. 8) confirm that in the off-equatorial regions, the northern zone has higher spectral power over all wavelengths, as expected from the EKEg spectra. Within the wavelength band from 100 to 250 km both off-equatorial regions have SSH spectral slopes between k^{-4} to k^{-5} (equivalent to k^{-2}-k^{-3} in EKE) similar to QG dynamics. The modelled SSH spectra show a similar anisotropy in the equatorial zone as the EKE spectra, with a more energetic meridional SSH spectrum than the zonal spectrum (not shown). Due to the strong ageostrophic component in the equatorial region, SSH spectra exhibit lower spectral power than in the off-equatorial region. From 100 to 600 km, the SSH spectral slopes in the equatorial region are close to k^{-4}, consistent with the k^{-2} spectral slopes in EKEg. The fixed wavelength band used by previous studies [70-250 km] can be compared to this longer wavelength band. Using the fixed wavelength band leads to a slight reduction in the low-frequency SSH spectral slope estimate, but without a drastic modification. These results indicate that if the internal balanced dynamics of our 1/12° model were the main contribution to the altimetric SSH, then we would expect a k^{-4} (sQG) slope in the equatorial band, and closer to k^{-5} (QG) in the off-equatorial band.

Fig. 8 also shows the alongtrack Topex/Poseidon SSH spectra over the same region and period as the G12d5 simulation. The altimetric data are selected with the same segment lengths, and with the same pre-processing and spectral filtering as in the model. In the equatorial and off-equatorial zones, the altimetric SSH wavenumber spectra clearly exhibit the weaker k^{-2}/k^{-1} spectral slopes in the 70-250 km mesoscale range as described in previous studies (Xu and Fu, 2011,2012; Zhou et al., 2015). At scales larger than our spectral slope range (600 km in the equatorial region, 200 km in the off-equatorial zones), the model-altimeter spectra have similar shapes although the altimeter data has higher spectral power. Potentially, the high-frequency < 10d rapid equatorial waves with longer wavelengths are not included in the model, and may contribute to these differences. The spectral peaks in the altimetric data at 120-150 km wavelength are indicative of internal tides, as noted by Dufau et al. (2016); Savage et al., (2017), and others. In addition to the internal tide peaks, the general higher spectral energy in the altimetry data at wavelengths < 200 km has been proposed to be due to high-frequency internal gravity waves (eg Richman et al., 2012, Savage et al., 2017), but may also include altimetric errors from surface waves and instrument noise (Dibarboure et al., 2014). We will investigate the high-frequency contribution to the altimetric SSH spectra in the next section.

Ocean Sci. Discuss., https://doi.org/10.5194/os-2018-49
Manuscript under review for journal Ocean Sci.
Discussion started: 28 June 2018
© Author(s) 2018. CC BY 4.0 License.

518 **5.2 Contributions from high-frequency dynamics including internal tides**

519 To investigate the contribution of the high-frequency SSH variations, we include an analysis of the
520 meridional SSH spectra from a small region east of the Solomon Sea in the SW Pacific. This spectral
521 analysis is derived from the 1/36° model with high-frequency atmospheric forcing and instantaneous
522 snapshots saved once per hour during a 3 month period, and run in the two configurations, with and
523 without tides (see section 2). The model has been validated and analysed (Djath et al., 2014), and a
524 companion paper will address the model with tides more fully (Tchilibou et al., 2018). Here we
525 consider specifically the impact of the different high-frequency tides and non-tidal signals on the
526 meridional SSH spectra.

527 The internal tide can be broken down into a coherent component that is predictable and can be
528 separated with harmonic and modal analysis, and an incoherent component that varies over time,
529 due to changing stratification (Zaron, 2017) or interaction with the mesoscale ocean circulation
530 (Ponte and Klein, 2015). The coherent baroclinic (internal) tide and the barotropic tide are calculated
531 in our study using a harmonic and modal decomposition (Nugroho, 2017) which separates the
532 barotropic mode and 9 internal tide modes, and provides a more stable energy repartition between
533 the baroclinic and barotropic components (F. Lyard, Personal Communication). Previous studies have
534 addressed the internal tide and high-frequency components in the tropics by careful filtering of a
535 model with tides (e.g. Richman et al., 2012; Savage et al., 2017). Aside from the issues of artifacts
536 introduced by the tidal filtering, it is often tricky to cleanly separate the spectral contributions
537 coming from the mesoscale ocean circulation and the incoherent component of the internal tides.
538 The advantage of using our two-model configuration is that we can specifically calculate the high-
539 frequency non-tidal components of the SSH spectra from the first model, and the component due to
540 the interaction of the internal tide and the model's eddy-current turbulence with the second model.

541 Fig.9 shows the geographical distribution of the standard deviation of SSH for the model including
542 the tidal forcing, for the low frequency (> 48 hr) component of the ocean (mesoscale) dynamics and
543 for the high frequency component (< 48 hr) due mainly to internal waves and internal tides. The large
544 mesoscale variability (up to 6 cm) east of the Solomon Sea in Fig. 9a is similar to the model without
545 tides (not shown), and well documented as current instability from the SECC-SEC current system (Qiu
546 and Chen, 2004). It is notable that the high frequency variability from the model with tides in Fig. 9b
547 is as high as the mesoscale variability, especially in the Solomon Sea, and comes mainly from the M2
548 baroclinic tide. We note that the M2 barotropic tide amplitude within the Solomon Sea is relatively
549 weak (not shown), and the largest internal tide amplitudes are close to their generation sites,
550 particularly where the barotropic tide interacts with the northern and southern Solomon Islands and
551 the southeastern Papua New Guinea (PNG) extremities (Tchilibou et al., 2018). For the model
552 without tides, the high frequency variability due to the atmospherically forced internal gravity waves
553 is very low (~1 cm) compared to the model with tides, and shows a relatively uniform distribution
554 (not shown).

555 The region used for our spectral analysis [2-13°S; 163-165°E; Fig. 9b] is outside the Solomon Sea, with
556 its strong regional circulation delimited by the islands and bathymetric gradients, and is more
557 representative of the open Pacific Ocean conditions analysed in the previous sections. The latitude
558 band from 2°S-13°S lies mostly the equatorial band defined in our previous analyses, and it is mainly
559 representative of the SECC region (Fig.3).

Ocean Sci. Discuss., https://doi.org/10.5194/os-2018-49
Manuscript under review for journal Ocean Sci.
Discussion started: 28 June 2018
© Author(s) 2018. CC BY 4.0 License.

The meridional SSH spectra from the 1/36° model run with no tides (R36h) with hourly outputs is shown in Fig. 10 (in green). The SSH from this version with no tides but averaged over 5 days is also shown (in orange), i.e., with equivalent temporal sampling to our 1/12° model analysis. The difference between these curves represents the non-tidal high-frequency component of the circulation (< 10 days) due to rapid tropical waves and internal gravity waves forced by the atmospheric forcing and current-bathymetric interactions. Also shown is the spectrum calculated at the same location from our open-ocean G12d5 1/12° model (in cyan) with similar spectral slope to the 5-day averaged version of our regional R36h 1/36° model, though with slightly lower energy at scales less than 70 km wavelength as expected, but also in the 180 to 600 km wavelength band. So the 1/36° model with no tides, when filtered to remove the high-frequency forcing, is quite close to the 1/12° model in this equatorial band. The main point is that the additional high-frequency dynamics in R36h increase the spectral SSH power from 300 km down to the smallest scales from 0.4 cm^2 to 0.5 cm^2, and reduce the spectral slope calculated in the fixed 70-250 km range from k^{-5} with the 5-day average (in orange), to k^{-4} for the full model with no tides (in green).

The 1/36° model with tides (R36Th) is also shown in blue, but with the barotropic tide removed. The additional meridional SSH spectral power is due both to the coherent and incoherent internal tides, with a large increase in variance up to 300 km wavelength from 0.5 cm^2 for R36h to 2.8 cm^2 for R36Th. So, the main contributors to the high wavenumber SSH spectral power are from the baroclinic tides compared to atmospherically-forced high frequency dynamics (green curve). To illustrate the respective part of coherent and incoherent baroclinic tides, the coherent baroclinic tide signature based on the nine tidal constituents summed over the first 9 internal modes is calculated, and this signal is added to the model without tides (purple curve). The coherent baroclinic tides explain most of the tidal signature in the 300-30 km wavelength range, and the difference with the raw signal (blue curve) exhibits the signature of incoherent tides. The contribution of the incoherent component increases significantly at scales smaller than 30 km and explain 30 % of the SSH variance. The most energetic coherent internal tide component comes from the M2 tide, and the large increase in amplitude centered around 120-140 km wavelength corresponds with the first baroclinic mode (not shown). The other peaks around 70 km, and 40 km could be due to higher modes, and similar peaks are found in the tidal analysis of MITGCM model data by Savage et al (2017) in the central equatorial Pacific. At the main M2 internal tide wavelengths, the incoherent internal tide has 1.6 times the SSH energy of the coherent tide, indicating that even at the main internal tide wavelengths, the incoherent internal tide is energetic.

We note that at wavelengths from 70-250 km used in the global altimetry spectral analysis, this 1/36° model with the full tidal and high-frequency forcing has a flat spectral peak of around $k^{-1.5}$, quite similar to the analysis of alongtrack spectral from Jason-2 (in dashed black) and Saral (in solid black), in the same region but over the longer 2013-2014 period. We note that the barotropic tide has also been removed from the altimetric data, using the same global tide atlas applied at the open boundary conditions for our regional model (FES2014, Lyard et al., 2018). If we use the “mesoscale” range defined for the global model analysis in the equatorial band over 100-600 km wavelength, we still have a weak spectral slope of k^{-2} for both the model with tides and altimetry. Jason-2 has a higher noise level than Saral at scales less than 30 km wavelength (Dufau et al., 2016); the small differences in spectral energy between Jason-2 and Saral over wavelengths from 150 to 450 km may be influenced by the different repetitive cycles of the very few tracks available (1 track for Jason-2 and 3 tracks for SARAL/AltiKA) between both missions, and their slightly different track positions.

© Author(s) 2018. CC BY 4.0 License.

This regional analysis provides a number of key results. The high-frequency, high-resolution regional model confirms our open ocean 1/12° analysis. The dynamics at scales > 10 days, with no tidal forcing, give rise to SSH spectral slopes from 70-250 km of around k^{-5} in this equatorial band in accordance with the G12d5 simulation. Note that it differs from the k^{-4} slope typical of the equatorial region discussed above. It reflects modulation associated with low frequency variability. This 3 month period corresponds with an El Niña event characterized by intense mesoscale activity in this region of the South West Pacific (Gourdeau et al., 2014). Including the high-frequency but non-tidal forcing increases the smaller-scale energy, and flattens the SSH spectra with slopes of around k^{-4}. This non-tidal high-frequency (< 10-day) component increases the SSH spectral energy out to scales of 200 km wavelength, suggesting a dominance of rapid small-scale eddy variability of internal gravity waves (Farrar and Durland, 2012; Garrett and Munk, 1975). But the higher frequency atmospheric forcing and ocean instabilities alone cannot explain the very flat altimetric spectral slopes in this equatorial region.

When coherent and incoherent internal tides are included, the spectral slope in the 70-250 km wavelength band becomes very close to that observed with altimetric spectra. This confirms the recent results presented by Savage et al. (2017) for a small box in the eastern tropics, and previously proposed by Richman et al. (2012) and Dufau et al. (2016). The separation of the coherent M2 internal tide demonstrates that it clearly contributes SSH energy in the 50-300 km wavelength band, but the incoherent tide, and its cascade of energy into the supertidal frequencies, is the dominant signal at scales less than 50 km. The incoherent and coherent internal tides have similar energy partitioning within the 50-300 km wavelength band.

6. Discussion and Conclusion

The processes that could contribute to the flat Sea Surface Height (SSH) wavenumber spectral slopes observed in the tropics by satellite altimetry have been examined in the tropical Pacific. This study has used two complementary approaches to better understand how the equatorial and off-equatorial dynamics impact on the SSH wavenumber spectra. In the first part of this study, we have concentrated on the low-frequency (> 10 days) internal tropical dynamics to better understand how the complex zonal current system and dominant linear tropical waves affect the mainly meridional altimetric SSH wavenumber spectra. In the second part of the study, we have used a high-frequency, high-resolution regional modeling configuration, with and without tides, to explore the high-frequency contributions to the meridional SSH wavenumber spectra.

Our 1/12°, 5-day averaged model confirms the results from previous modeling studies that at seasonal to interannual time scales the most energetic large-scale structures tends to be anisotropic and governed by linear dynamics. At intraseasonal frequencies and in the tropical “mesoscale” band at scales less than 600 km wavelength, one major question was how the cascade of energy is affected by the expected high level of anisotropy and the weak non-linear regimes. Within the “mesoscale” range, the EKE wavenumber spectra is isotropic in the off-equatorial regions between 10° and 20°, and it is more anisotropic in the equatorial region between 10°N-10°S, with higher level of energy for the meridional EKE spectrum than for the zonal one that reveals the energetic meridional perturbations due to instabilities of the larger-scale zonal currents.

© Author(s) 2018. CC BY 4.0 License.

645 In the off-equatorial range, EKE peaks at around 300 km wavelength, and the steep EKE decrease at
646 smaller wavelength is characterized by spectral slopes between k^{-2} and k^{-3}, which lie between the
647 regimes of SQG and QG turbulence. These weakly nonlinear off-equatorial regions thus have a similar
648 structure to the non-linear mid-latitudes within the range from 100-250 km. In the equatorial band
649 from 10°S-10°N, the total EKE is more energetic than the off-equatorial region, and the spectral
650 cascade extends over a large wavenumber range, from 100 to 600 km. Again, the EKE spectral slope
651 within this range approaches k^{-3}, consistent with QG dynamics, even though there is a strong
652 ageostrophic component here. Using the fixed wavelength (70-250 km) band to estimate
653 "mesoscale" spectral slope leads to a slight reduction in the low-frequency spectral slope estimate,
654 but without a drastic modification. When geostrophic velocities are used to calculate EKE rather than
655 the total surface flow, there is similar spectral energy in the off-equatorial regions at longer
656 wavelengths. In the equatorial band 10°N-10°S, the ageostrophy is more evident with a more marked
657 change in spectral slope based on geostrophic velocities and the beta-approximation at the equator.
658 At large scales in the equatorial band, the ageostrophic equatorial currents are more active, related
659 to the energetic zonal currents. In all regions, at wavelengths shorter than 200 km, the geostrophic
660 spectra become more energetic and the small-scale ageostrophic components are counteracting the
661 balanced geostrophic flow, as found at mid-latitudes (Klein et al., 2008). This gives a slightly flatter
662 spectral slope over the 70-250 km wavelength, but the regime remains between k^{-2} and k^{-3} in the off-
663 equatorial region, approaching k^{-2} (and k^{-4} in SSH) in the equatorial band. So using SSH and
664 geostrophic currents slightly flattens the wavenumber spectra, but cannot explain alone the very flat
665 altimetric SSH spectra.

666 The choice of regional box size and filtering options also impacts on the spectra. Previous global
667 altimetric studies have calculated alongtrack SSH wavenumber spectra in 10x10° boxes, and with
668 varying segment lengths (512 km for Dufau et al., 2016; around 1000 km for Xu and Fu, 2011,
669 Chassignet et al., 2017, etc), and with different tapering or filtering applied (see section 3). In the
670 equatorial band where the EKE peak extends out to 600 km wavelength, it is important to have
671 segment sizes and filtering that preserve this peak and shorter scales. The combined effects of a 10%
672 cosine taper and the short segment lengths leads to a much flatter altimetric SSH spectra, reaching k^{-1}
673 in the Dufau et al (2016) study. We find that the double periodic spectra, the hanning and tukey
674 50% taper filter all give similar results in the tropics, but it is necessary to extend the box size to a
675 minimum of 15° to 20° in segment length or box size in the equatorial band. In the off-equatorial
676 band, these filtering options with a 10° segment length or box size are sufficient. Even with the
677 preferred pre-processing for the altimetric data, and larger segment lengths in our analyses, the
678 altimetric SSH spectra remain quite flat (k^{-2} in the off-equatorial zone, $k^{-1.3}$ in the equatorial band),
679 and do not reflect the steeper, more turbulent spectral slopes predicted by the model.

680 The regional high-resolution models with both high-frequency atmospheric and tidal forcing and
681 high-frequency hourly outputs provide the last pieces of the puzzle. In contrast to previous results
682 based on global ocean models with tidal forcing (Richman et al., 2012; Savage et al., 2017), this 2-
683 model configuration with and without tides, has the same atmospheric and boundary forcing, which
684 allows us to clearly separate the internal tide signals from the high frequency dynamical component.
685 Even though only a small region of the tropical Pacific is available for this analysis, the regional model
686 and the global 1/12° model show similar QG spectral slopes when they are compared over the same
687 domain and with 5-day averaged data. Using hourly data and no tides increases the SSH spectral
688 power at scales smaller than 200 km, possibly due to internal gravity waves in the tropics (Farrar and

© Author(s) 2018. CC BY 4.0 License.

Durland, 2012; Garrett and Munk, 1975). We note that Rocha et al. (2016) found a similar increase in their detided alongtrack model runs in Drake Passage, but at scales less than 40 km wavelength, far below the noise level of our present altimeter constellation. In the tropics, this contribution of high-frequency non-tidal SSH signals out to 200 km wavelength will also impact on today's alongtrack altimeter constellation, whose noise levels block ocean signals at scales less than 70 km for Jason class satellites, and 30-50 km for Saral and Sentinel-3 SAR altimeters (Dufau et al., 2016). So non-tidal internal gravity waves will partially contribute to the higher small-scale SSH variance and flatter spectral slopes in today's altimetric SSH data.

The regional model with tides shows the very important contribution of internal tides to the flat SSH slopes in the tropics. We have separated out the predictive part of the barotropic tide and internal tides, since open ocean barotropic tides are well corrected for in altimetric data today (Lyard et al., 2018; Stammer et al., 2014), and corrections are becoming available for the coherent part of the internal tide (Ray and Zaron, 2016). In this open ocean tropical region east of the Solomon Sea, when coherent and incoherent internal tides are included, the spectral slope in the 70-250 km wavelength band becomes very close to that observed with altimetric spectra. This confirms the recent results presented by Savage et al. (2017) for a small box in the eastern tropics, and previously proposed by Richman et al. (2012) and Dufau et al. (2016). The separation of the coherent M2 internal tide demonstrates that it clearly contributes significant SSH energy in the 50-300 km wavelength band, but around the main internal tide wavelengths, there is a strong signature of M2 incoherent internal tide. The incoherent tide, and its cascade of energy into the supertidal frequencies, is the dominant signal at scales less than 50 km. This strong incoherent internal tide is consistent with recent studies that suggest that internal tides interacting with energetic zonal jets can generate a predominate incoherent internal tide (Ponte and Klein, 2015), and may explain the reduction of the coherent internal tides in the equatorial band in global models (Shriver et al., 2014) and altimetric analyses (Ray and Zaron, 2016). Our model highlights that the internal tide signal is strong in this equatorial region, and the incoherent tide accounts for 35% of the SSH spectral power in the 50-300 km wavelength band, and is not predictable.

These results have important consequences for the analyses of alongtrack altimetric data today, and for the future high-resolution swath missions such as SWOT. Today's constellation of satellite altimeters have their alongtrack data filtered to remove noise at scales less than 70 km for all missions (Dibarboure et al., 2014; Dufau et al., 2016), and these data are now being used with no internal tide correction in the global gridded altimetry maps of SSH and geostrophic currents. The imprint of these internal tides is evident in the alongtrack data (see Fig. 1b from Dufau et al., 2016) but is also present in the gridded maps (R. Ray, personal communication). In the future, a coherent internal tide correction may be applied to the alongtrack data based on Ray and Zaron (2016), to reduce some of this non-balanced signal. It is particularly important to remove the unbalanced internal wave signals from SSH before calculating geostrophic currents. But it is clear that the incoherent internal tide and internal gravity waves reach scales of 200 km in the tropics, and their signature in SSH remains a big issue for detecting balanced internal ocean currents from alongtrack altimetry and the future SWOT wide-swath altimeter mission. Removing this signal to detect purely balanced motions will be challenging, since filtering over 200 km removes much of the small-scale ocean dynamics of interest in the tropics. On the other hand, there will also be a great opportunity to investigate the interaction of the internal tide and ocean dynamics in the tropics in the future, with both models and fine-scale altimetric observations.

© Author(s) 2018. CC BY 4.0 License.

Acknowledgments

The authors wish to acknowledge Ssalto/Duacs AVISO who produced the altimeter products, with support from CNES (http://www.aviso.altimetry.fr/duacs/). The authors would like to thank the DRAKKAR team for providing them with the high resolution global ocean simulation, and especially J.M. Molines for his support. This work benefited from discussions with J. Jouanno, F. Marin, Y. Morel from LEGOS. We particularly thank J. Verron (IGE), C. Menesguen (LOPS), and X. Capet (LOCEAN) for their time, and their fruitful comments. M. Tchilibou is funded by Université de Toulouse 3. L. Gourdeau, G. Sérazin are funded by IRD; R. Morrow is funded by CNAP, and B. Djath was funded by CNES. This work is a contribution to the joint CNES/NASA SWOT project "SWOT in the tropics" and is supported by the French TOSCA programme.

References

Adcroft, A., Hill, C., and Marshall, J.: Representation of topography by shaved cells in a height coordinate ocean model, Mon. Weather Rev., 125, 2293-2315, 1997.

Barnier B., Madec, G., Penduff, T., Molines, J.-M., Treguier, A.-M., Le Sommer, J., Beckmann, A., Biastoch, A., Böning, C., Dengg, J., Derval, C., Durand, E., Gulev, S., Remy, E., Talandier, C., Theetten, S., Maltrud, M., McClean, J., and De Cuevas, B.: Impact of partial steps and momentum advection schemes in a global ocean circulation model at eddy permitting resolution. Ocean Dynamics, Vol 4, DOI: 10.1007/s10236-006-0082-1, 2006.

Biri, S., Serra, N., Scharffenberg, M.G., Stammer, D.: Atlantic sea surface height and velocity spectra inferred from satellite altimetry and a hierarchy of numerical simulations, J. of Geophys. Res.: Oceans 121 (6), 4157-4177, doi: 10.1002/2015JC011503, 2016.

Capet, X., Klein, P., Hua, B., Lapeyre, G., and McWilliams, J. C.: Mesoscale to submesoscale transition in the California Current system. Part III: Energy balance and flux. J. Phys. Oceanogr., 38, 2256-2269, 2008.

Carrere, L., and Lyard, F.: Modeling the barotropic response of the global ocean to atmospheric wind and pressure forcing - comparisons with observations, Geophys. Res. Lett., 30, 1275, doi:10.1029/2002GL016473, 6, 2003.

Chassignet, E.P. and Xu, X.: Impact of horizontal resolution (1/12° to 1/50°) on Gulf Stream separation, penetration, and variability. J. Phys. Oceanogr., 47, 1999-2021, doi:10.1175/JPO-D-17-0031.1, 2017.

Chelton, D. B., DeSzoeke, R. A., Schlax, M. G., El Naggar, K., and Siwertz, N.: Geographical variability of the first baroclinic Rossby radius of deformation, J. Phys. Oceanogr., 28, 433-460, 1998.

Chelton, D. B., Schlax, M. G., Samelson, R. M., and De Szoeke, R. A.: Global observations of westward energy propagation in the ocean: Rossby waves or nonlinear eddies?, Geophys. Res. Lett., 34, L15606, doi:10.1029/2007GL030812, 2007.

Cravatte, S., Picaut, J., and Eldin, G.: Second and first baroclinic Kelvin modes in the equatorial Pacific at intraseasonal timescales, J. Geophys. Res., 108(C8), 3266, doi:10.1029/2002JC001511, 2003.

Dee, D. P., Uppala, S. M., Simmons, A. J., Berrisford, P., Poli, P., Kobayashi, S., Andrae, U., Balmaseda, M. A., Balsamo, G., Bauer, P., Bechtold, P., Beljaars, A. C. M., van de Berg, L., Bidlot, J., Bormann, N., Delsol, C., Dragani, R., Fuentes, M., Geer, A. J., Haimberger, L., Healy, S. B., Hersbach, H., Helm, E. V., Isaksen, L., Kallberg, P., Kahler, M., Matricardi, M., McNally, A. P., Monge-Sanz, B. M., Morcrette, J.-J., Park, B.-K., Peubey, C., de Rosnay, P., Tavolato, C., Thepaut, J.-N. and Vitart, F.: The ERA-Interim reanalysis: configuration and performance of the data assimilation system. Q.J.R. Meteorol. Soc., 137: 553-597. doi:10.1002/qj.828, 2011.

© Author(s) 2018. CC BY 4.0 License.

Dibarboure, G., Boy, F., Desjonqueres, J. D., Labroue, S., Lasne, Y., Picot, N., Poisson ,J. C., and Thibaut P.: Investigating short-wavelength correlated errors on low-resolution mode altimetry. Journal of Atmospheric Oceanic Technology, 31:1337-1362, 2014.

Djath, B., Verron, J., Melet, A., Gourdeau, L., Barnier, B., and Molines, J.-M.: Multiscale dynamical analysis of a high-resolution numerical model simulation of the Solomon Sea circulation, J. Geophys. Res. Oceans, 119, doi:10.1002/2013JC009695, 2014.

Dufau, C., Orsztynowicz, M., Dibarboure, G., Morrow, R., and Le Traon, P.-Y.: Mesoscale resolution capability of altimetry: Present and future, J. Geophys. Res. Oceans, 121, 4910-4927, doi:10.1002/2015JC010904, 2016.

Eden, C.: Eddy length scales in the North Atlantic Ocean, J. Geophys. Res., 112, C06004, doi:10.1029/2006JC003901, 2007.

Farrar, J. T.: Observations of the dispersion characteristics and meridional sea level structure of equatorial waves in the Pacific Ocean. J. Phys. Oceanogr., 38, 1669-1689, 2008.

Farrar, J.T., and Durland, T.S.: Wavenumber-frequency spectra of inertia-gravity and mixed Rossby-gravity waves in the equatorial Pacific Ocean. J. Phys. Oceanogr., 42, 1859-1881, 2012.

Fu, L.: Latitudinal and Frequency Characteristics of the Westward Propagation of Large-Scale Oceanic Variability. J. Phys. Oceanogr., 34, 1907-1921, https://doi.org/10.1175/1520-0485(2004)034<1907:LAFCOT>2.0.CO;2, 2004.

Fu, L.-L.: Pattern and velocity of propagation of the global ocean eddy variability, J. Geophys. Res., 114, C11017, doi:10.1029/2009JC005349, 2009.

Fu, L. and Ubelmann, C.: On the Transition from Profile Altimeter to Swath Altimeter for Observing Global Ocean Surface Topography. J. Atmos. Oceanic Technol., 31, 560-568, https://doi.org/10.1175/JTECH-D-13-00109.1, 2014.

Ganachaud, A., et al.: The Southwest Pacific Ocean circulation and climate experiment (SPICE), J. Geophys. Res. Oceans, 119, doi:10.1002/2013JC009678, 2014.

Garrett, C., and Munk, W.: Space-time scales of internal waves: A progress report, J. Geophys. Res., 80, 291–297, doi:10.1029/JC080i002p00291, 1975.

Gourdeau, L.: Internal tides observed at 2°S-156°E by in situ and TOPEX/POSEIDON data during COARE, J. Geophys. Res., 103, 12,629-12,638, 1998.

Gourdeau, L., Verron, J., Melet, A., Kessler, W., Marin, F., and Djath B.: Exploring the mesoscale activity in the Solomon Sea: a complementary approach with numerical model and altimetric data, J. Geophys. Res. Oceans, 119, 2290-2311, doi:10.1002/2013JC009614, 2014.

Gourdeau, L., Verron, J., Chaigneau, A., Cravatte, S., and Kessler, W.: Complementary use of glider data, altimetry, and model for exploring mesoscale eddies in the tropical Pacific Solomon Sea. Journal of Geophysical Research: Oceans, 122. https://doi.org/10.1002/2017JC013116, 2017.

Hristova, H. G., Kessler, W. S., McWilliams, J. C., and Molemaker, M. J.: Mesoscale variability and its seasonality in the Solomon and Coral Seas, J. Geophys. Res. Oceans, 119,4669–4687, doi:10.10022013JC009741, 2014.

Hughes, C. W., and Williams, S. D. P.: The color of sea level: Importance of spatial variations in spectral shape for assessing the significance of trends, J. Geophys. Res., 115, C10048, doi:10.1029/2010JC006102, 2010.

Kennan, S.C., and Flament, P.J. : Observations of a tropical instability vortex. Journal of Physical Oceanography 30 (9), 2277-2301, 2000.

Kessler, W. S., McPhaden, M. J., and Weikmann, K. M.: Forcing of intraseasonal Kelvin waves in the equatorial Pacific, J. Geophys. Res., 100, 10,613 - 10,631, 1995.

Klein, P., Hua, B., Lapeyre, G., Capet, X., Gentil, S. L., and Sasaki, H.: Upper ocean turbulence from high 3-d resolution simulations. J. Phys. Oceanogr., 38, 1748-1763, 2008.

Klocker, A., and Abernathey, R.: Global Patterns of Mesoscale Eddy Properties and Diffusivities. J. Phys. Oceanogr., 44, 1030-1046, https://doi.org/10.1175/JPO-D-13-0159.1, 2014.

Klocker, A., Marshall, D. P., Keating, S. R., and Read, P. L.: A regime diagram for ocean geostrophic turbulence. Q.J.R. Meteorol. Soc., 142: 2411-2417, 2016.

© Author(s) 2018. CC BY 4.0 License.

830 Kobashi, F., and Kawamura, H.: Seasonal variation and instability nature of the North Pacific
831 Subtropical Countercurrent and the Hawaiian Lee Countercurrent, J. Geophys. Res., 107(C11),
832 3185, doi:10.1029/2001JC001225, 2002.
833 Lambin J., Morrow, R., Fu, L. L., Willis, J. K., Bonekamp, H., Lillibridge, J., Perbos, J. , Zaouche, G., Vaze,
834 P., Bannoura, W., Parisot, F., Thouvenot, E., Coutin-Faye, S., Lindstrom, E., and Mignogno, M.:
835 The OSTM/Jason-2 Mission, Marine Geodesy, 33:S1, 4-25, DOI: 10.1080/01490419.2010.491030,
836 2010.
837 Large, W., and Yeager, S.: Diurnal to decadal global forcing for ocean and sea-ice models: The data
838 sets and Flux climatologies. In Climate and global dynamics division (Tech. Note NCAR/TN-
839 4601STR). Boulder, CO: The National Center for Atmospheric Research.
840 https://doi.org/10.5065/D6KK98Q6, 2004.
841 Large, W., and Yeager, S.: The global climatology of an interannually varying air-sea flux data set,
842 Clim. Dyn., 33, 341-364, 2009.
843 Lecointre, A., Molines, J.-M.,and Barnier, B. : Definition of the interannual experiment ORCA12.L46-
844 MAL95, 1989-2007 (Internal Rep. MEOM-LEGI-CNRS, LEGI-DRA-21-10-2011, 25 p.). Grenoble,
845 France: Drakkar, 2011.
846 Le Traon, P.Y., Klein, P., Hua, B.L., and Dibarboure, G.: Do Altimeter Wavenumber Spectra Agree with
847 the Interior or Surface Quasigeostrophic Theory?. J. Phys. Oceanogr., 38, 1137-1142,
848 https://doi.org/10.1175/2007JPO3806.1, 2008.
849 Levitus, S., Boyer, T. P., Conkright, M. E., O'Brien, T., Antonov, J., Stephens, C., Gelfeld, R.: NOAA Atlas
850 NESDIS 18,World Ocean Data base 1998: VOLUME 1: Introduction (346 pp.). Washington, DC:
851 U.S. Gov. Printing Office, 1998.
852 Lin, X., Yang, J., Wu, D., and Zhai, P.: Explaining the global distribution of peak-spectrum variability of
853 sea surface height, Geophys. Res. Lett., 35, L14602, doi:10.1029/2008GL034312, 2008.
854 Lyard, F. , Cancet, M., Carrere, L., Allain, D.: FES2014 global ocean tides atlas: design and
855 performances, Ocean Dynamics (in preparation)
856 Lyman, J.M., Johnson, G.C., Kessler, and W.S.: Distinct 17- and 33-day tropical instability waves in
857 subsurface observations. Journal of Physical Oceanography, 37 (4), 855-872, 2007.
858 Madec, G.: NEMO ocean engine, Note du Pole de Mod_lisation, Tech. Rep. 27, 300 pp., Inst. Pierre
859 Simon Laplace, France, 2008.
860 Marchesiello, P., Capet, X., Menkes, C., and Kennan, S.C.: Submesoscale dynamics in tropical
861 instability waves. Ocean Modell. 39 (1-2), 31-46. doi:10.1016/j.ocemod.2011.04.011, 2011.
862 Masina, S., Philander, S. G. H., and Bush, A. B. G.: An analysis of tropical instability waves in a
863 numerical model of the Pacific Ocean: 2. Generation and energetics of the waves, J. Geophys.
864 Res., 104(C12), 29637-29661, doi:10.1029/1999JC900226, 1999.
865 Morten, A.J., Arbic, B.K., and Flierl, G.R.: Wavenumber-frequency analysis of single-layer shallow-
866 water beta-plane quasi-geostrophic turbulence, Physics of Fluids, 29, 106602,
867 doi:10.1063/1.5003846, 2017.
868 Niwa, Y., and Hibiya, T.: Estimation of baroclinic tide energy available for deep ocean mixing based on
869 three-dimensional global numerical simulations. J. Oceanogr., 67, 493-502,
870 doi:https://doi.org/10.1007/s10872-011-0052-1, 2011.
871 Nugroho, D.: The Tides in a general circulation model in the Indonesian Seas . Ocean, Atmosphere.
872 Universite Toulouse 3 Paul Sabatier (UT3 Paul Sabatier), 2017.
873 Penduff, T., Le Sommer, J., Barnier, B., Treguier, A.-M., Molines, J.-M., and Madec, G.: Influence of
874 numerical schemes on current topography interactions in 1/48 global ocean simulations. Ocean
875 Science, 3, 509-524. https://doi.org/10.5194/os-3-509-2007, 2007.
876 Picaut, J., Hayes, S. P., and McPhaden, M. J.: Use of the geostrophic approximation to estimate time-
877 varying zonal currents at the equator, J. Geophys. Res., 94(C3), 3228-3236,
878 doi:10.1029/JC094iC03p03228, 1989.
879 Ponte, A. L., and Klein, P.: Incoherent signature of internal tides on sea level in idealized numerical
880 simulations, Geophys. Res. Lett., 42, 1520-1526, doi:10.1002/2014GL062583, 2015.

© Author(s) 2018. CC BY 4.0 License.

881 Qiu, B., and Chen, S.: Seasonal modulation in the eddy field of the South Pacific Ocean. J. Phys. Qiu,
882 B., R.B. Scott, and S. Chen, 2008: Length Scales of Eddy Generation and Nonlinear Evolution of
883 the Seasonally Modulated South Pacific Subtropical Countercurrent. J. Phys. Oceanogr., 38,
884 1515–1528, https://doi.org/10.1175/2007JPO3856.1, 2004.
885 Ray, R.D., and Zaron, E.D.: M_2 Internal Tides and Their Observed Wavenumber Spectra from Satellite
886 Altimetry. J. Phys. Oceanogr., 46, 3–22, https://doi.org/10.1175/JPO-D-15-0065.1, 2016.
887 Rocha, C.B., Chereskin, T.K., Gille, S.T., and Menemenlis, D.: Mesoscale to Submesoscale
888 Wavenumber Spectra in Drake Passage. J. Phys. Oceanogr., 46, 601-620,
889 https://doi.org/10.1175/JPO-D-15-0087.1, 2016.
890 Rhines, P. B.: Waves and turbulence on a beta-plane. J. Fluid Mech., 69, 417-443, 1975.
891 Richman, J. G., Arbic, B. K., Shriver, J. F., Metzger, E. J., and Wallcraft, A. J.: Inferring dynamics from
892 the wavenumber spectra of an eddying global ocean model with embedded tides, J. Geophys.
893 Res., 117, doi:10.1029/2012JC008364, 2012.
894 Sasaki, H., and Klein, P.: SSH wavenumber spectra in the North Pacific from a high-resolution realistic
895 simulation, J. Phys. Oceanogr., 42, 1233-1241, doi:10.1175/JPO-D-11-0180.1, 2012.
896 Sasaki, H., and Nonaka, M.: Far-reaching Hawaiian Lee Countercurrent driven by wind-stress curl
897 induced by warm SST band along the current. Geophys. Res. Lett., 33, L13602,
898 doi:10.1029/2006GL026540, 2006.
899 Savage, A. C., et al.: Frequency content of sea surface height variability from internal gravity waves to
900 mesoscale eddies, J. Geophys. Res. Oceans, 122, 2519-2538, doi:10.1002/2016JC012331, 2017.
901 Shriver, J. F., Richman, J. G., and Arbic, B. K.: How stationary are the internal tides in a high resolution
902 global ocean circulation model?, J. Geophys. Res. Oceans, 119, 2769â€“2787,
903 doi:10.1002/2013JC009423, 2014.
904 Soufflet Y., Marchesiello, P., Lemarie, F., Jouanno, J., Capet, X., Debreu, L., Benshila, R. : On effective
905 resolution in ocean models. Ocean Modelling, 98, 36-50. ISSN 1463-5003, 2016.
906 Stammer, D., et al.: Accuracy assessment of global barotropic ocean tide models, Rev. Geophys., 52,
907 243–282, *doi:* 10.1002/2014RG000450, 2014.
908 Stammer, D.: Global characteristics of ocean variability estimated from regional TOPEX/POSEIDON
909 altimeter measurements, J. Phys. Oceanogr., 27, 1743 – 1769, 1997.
910 Tchilibou, M., Gourdeau, L., Djath, B., Lyard, F., Allain, D., Morrow, R.: Internal tide in the Solomon
911 Sea, PS44A-2299, Ocean Science meeting, 11-16 Feb., Portland, 2018.
912 Theiss, J.: Equatorward energy cascade, critical latitude, and the predominance of cyclonic vortices in
913 geostrophic turbulence, J. Phys. Oceanogr., 34, 1663 – 1678, 2004.
914 Treguier, A. M., Barnier, B., deMiranda, A. P., Molines, J. M., Grima, N., Imbard, M., Madec, G.,
915 Messager, C., Reynaud, T., and Michel, S.: An eddy-permitting model of the Atlantic circulation:
916 Evaluating open boundary conditions, J. Geophys. Res., 106(C10), 22115-22129,
917 doi:10.1029/2000JC000376, 2001.
918 Tulloch, R., Marshall, J., and Smith, K. S.: Interpretation of the propagation of surface altimetric
919 observations in terms of planetary waves and geostrophic turbulence, J. Geophys. Res., 114,
920 C02005, doi:10.1029/2008JC005055, 2009.
921 Ubelmann, C., and Fu, L.L.: Vorticity structures in the tropical Pacific from a numerical simulation. J.
922 Phys. Oceanogr., 41, 1455-1464, doi 10.1175/2011JPO4507.1, 2011.
923 Verron, J., and Blayo, E.: The no-slip boundary condition and the Gulf Stream separation problem.
924 Journal of Physical Oceanography, 26(9), 1938-1951. https://doi.org/10.1175/1520-0485, 1996.
925 Verron J., Sengenes, P., Lambin, J., Noubel, J., Steunou, N., Guillot, A., Picot, N., Coutin-Faye, S.,
926 Sharma, R., Gairola, R. M., Raghava Murthy, D. V. A., Richman, J. G., Griffin, D., Pascual, A., Rémy
927 F., and Gupta, P. K.: The SARAL/AltiKa Altimetry Satellite Mission, Marine Geodesy, 38:sup1, 2-
928 21, DOI: 10.1080/01490419.2014.1000471, 2015.
929 Wakata, Y.: Frequency wavenumber spectra of equatorial waves detected from satellite altimter
930 data, J. Oceanogr., 63, 483-490, doi: 10.1007/s10872-007-0043-4, 2007.

© Author(s) 2018. CC BY 4.0 License.

931 Willett, C. S., Leben, R. R., and Lavin, M. F.: Eddies and tropical instability waves in the eastern
932 tropical Pacific: A review. Prog. Oceanogr., 69, 218-238, doi:10.1016/j.pocean.2006.03.010,
933 2006.
934 Wortham, J.C., and Wunsch, C.: A multidimensional spectral description of ocean variability. J. Phys.
935 Oceanogr., 44, 944-966, doi: 10.1175/JPO-D-13-0113.1, 2014.
936 Wunsch, C.: Towards a mid-latitude ocean frequency-wavenumber spectral density and trend
937 determination, J. Phys. Oc., 40, 2264-2281, 2010.
938 Xu, Y., and Fu, L.-L.: Global variability of the wavenumber spectrum of oceanic mesoscale turbulence.
939 J. Phys. Oceanogr., 41, 802-809, 2011.
940 Xu, Y. and Fu L.-L.: The Effects of Altimeter Instrument Noise on the Estimation of the Wavenumber
941 Spectrum of Sea Surface Height. J. Phys. Oceanogr., 42, 2229-2233,
942 https://doi.org/10.1175/JPO-D-12-0106.1, 2012.
943 Zaron, E. D.: Mapping the nonstationary internal tide with satellite altimetry, J. Geophys. Res.
944 Oceans, 122, 539-554, doi:10.1002/2016JC012487, 2017.
945 Zhou, X.-H., Wang D.-P., and Chen, D.: Global wavenumber spectrum with corrections for altimeter
946 high-frequency noise, Journal of Physical Oceanography 45.2, 495-503, 2015.
947

Ocean Sci. Discuss., https://doi.org/10.5194/os-2018-49
Manuscript under review for journal Ocean Sci.
Discussion started: 28 June 2018
© Author(s) 2018. CC BY 4.0 License.

Figure captions

Figure 1: a) Spatial distribution of altimetric alongtrack SSH wavenumber spectral slope calculated in the fixed 70-250 km mesoscale range (from Xu and Fu, 2011; their Fig. 2). b) Latidudinal dependence of the altimetric SSH alongtrack wavenumber spectra in the Atlantic Ocean (from Dufau et al., 2016; their Fig. 3). The colors of the spectra refer to the geographical boxes where alongtrack data were averaged on the right.

Figure 2: Sensitivity experiments for different spectral processing techniques applied to meridional SSH wavenumber spectra representative of the equatorial region. a) SSH wavenumber spectra using a Tukey 0.1 window (blue) and a Tukey 0.5 window (red) depending on segment lengths: 5° (dots), 10° (dash), 20° (line). b) SSH wavenumber spectra using different windowing over a 20° segment length: Tukey 0.1 window (Tk01, blue), Tukey 0.5 window (Tk05, red), Hanning window (Han, green). The double periodic method (Dbp, black) is also tested. For reference k^{-1} and k^{-5} curves are plotted. Units : $cm^2/cpkm$

Figure 3: Snapshot of relative vorticity of the 1/12° G12d5 simulation. unit in 1.E5 s^{-1}. The yellow lines delineate the equatorial and off-equatorial regions. The dashed lines delineate square boxes for the different regions to compute wavenumber spectra. The black arrows illustrate the main zonal tropical currents (SEC: South Equatorial Current, SECC: South Equatorial CounterCurrent, NECC: North Equatorial CounterCurrent, NEC: North Equatorial Current, STCC: SubTropical CounterCurrent, HLCC: Hawaiin Lee Counter Current).

Figure 4: a) latitudinal distribution of the EKE Frequency power spectra computed at each model grid point of the G12d5 simulation, and averaged in longitude. The black line is the critical period from Lin et al. (2008). b) longitudinal distribution of the EKE Frequency power spectra computed at each model grid point of the G12d5 simulation, and averaged between 20°S-20°N. Units are in log_{10} of $cm^2/s^2/cpday$.

Figure 5: Zonal wavenumber-frequency EKE spectra averaged over a) 10°N-20°N region, b) 10°S-10°N region, and c) 10°S-20°S region. d) Meridional wavenumber-frequency EKE spectra covering 20°S-20°N averaged over the 120°W-150°W region. Superimposed on a) and c) are the theoretical dispersion curves for the first mode baroclinic waves. Superimposed on b) are the theoretical dispersion curves for the first 3 baroclinic wave modes, and the Kelvin wave mode. Units are in log_{10} of $cm^2/s^2/cpday/cpkm$.

Figure 6: Zonal wavenumber EKE spectra averaged over the equatorial (orange line), and off-equatorial latitude bands (north: green; south: blue). Units are in $cm^2/s^2/cpkm$.

Figure 7: 1D zonal (orange), meridional (green); and 2D isotropic (blue) EKE wavenumber spectra averaged over a) 10°N-20°N, b) 10°S-10°N, and c) 10°S-20°S regions. The isotropic geostrophic EKE wavenumber spectra is also shown (EKEg, blue dash line). The vertical green dash lines delineate the fixed 70-250 km mesoscale range. For reference, k^{-2} and k^{-3} curves are plotted (black lines). Units are in $cm^2/s^2/cpkm$.

Ocean Sci. Discuss., https://doi.org/10.5194/os-2018-49
Manuscript under review for journal Ocean Sci.
Discussion started: 28 June 2018
© Author(s) 2018. CC BY 4.0 License.

Figure 8: Meridional SSH wavenumber spectra averaged over the equatorial (orange), and off-equatorial latitude bands (north: green, south:blue) for the G12d5 simulation (line). Topex-Poseidon along track altimetric SSH wavenumber spectra are averaged over the same latitude bands (dash). Units are in cm^2/cpkm.

Figure 9: SSH variability of the 1/36° regional model with explicit tides (R36Th) over the 3 month simulation for a) the mesoscale signal, and b) the internal waves and internal tides defined by a 48 hr cutoff period. Units in cm^2. The SARAL/AltiKA (black line) and Jason-2 (dash line) tracks used to compute the altimetric spectra in Fig. 10 are superimposed.

Figure 10: Meridional SSH wavenumber spectra averaged over 163°E-165°E for the hourly outputs of the 1/36° resolution regional model without tides (R36h, green), and 5 day averaged outputs (R36d5, orange). Meridional SSH spectra of the G12d5 simulation is in cyan. SSH meridional wavenumber spectra for the hourly outputs of the 1/36° regional model with explicit tides once the barotropic tides has been removed (R36Th-BT, in blue). The spectrum of the coherent baroclinic tides has been added to the spectrum of the model without tides (R36h+BC, purple), the contribution of the only M2 coherent baroclinic tide is in red (R36h+M2BC). The difference between the blue and purple curves corresponds with the incoherent internal tides. The corresponding along track SSH altimetric spectra for SARAL/AltiKa (line) and Jason-2 (dash) are in black. Units are in cm^2/cpkm.

Ocean Sci. Discuss., https://doi.org/10.5194/os-2018-49
Manuscript under review for journal Ocean Sci.
Discussion started: 28 June 2018
© Author(s) 2018. CC BY 4.0 License.

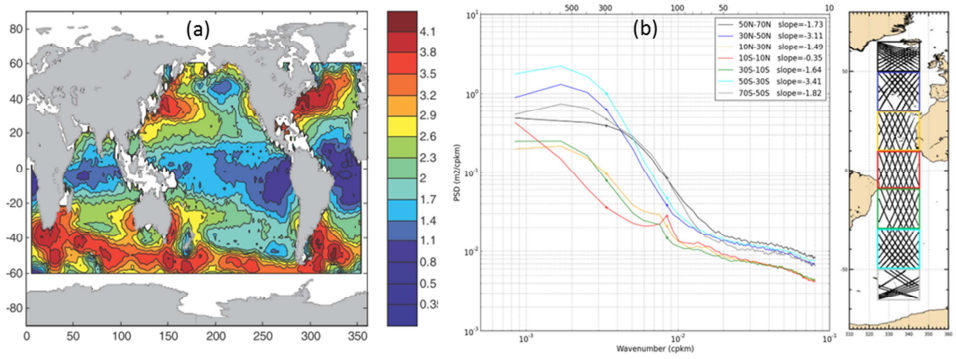

Figure 1: a) Spatial distribution of altimetric alongtrack SSH wavenumber spectral slope calculated in the fixed 70-250 km mesoscale range (from Xu and Fu, 2011; their Fig. 2). b) Latidudinal dependence of the altimetric SSH alongtrack wavenumber spectra in the Atlantic Ocean (from Dufau et al., 2016; their Fig. 3). The colors of the spectra refer to the geographical boxes where alongtrack data were averaged on the right.

Ocean Sci. Discuss., https://doi.org/10.5194/os-2018-49
Manuscript under review for journal Ocean Sci.
Discussion started: 28 June 2018
© Author(s) 2018. CC BY 4.0 License.

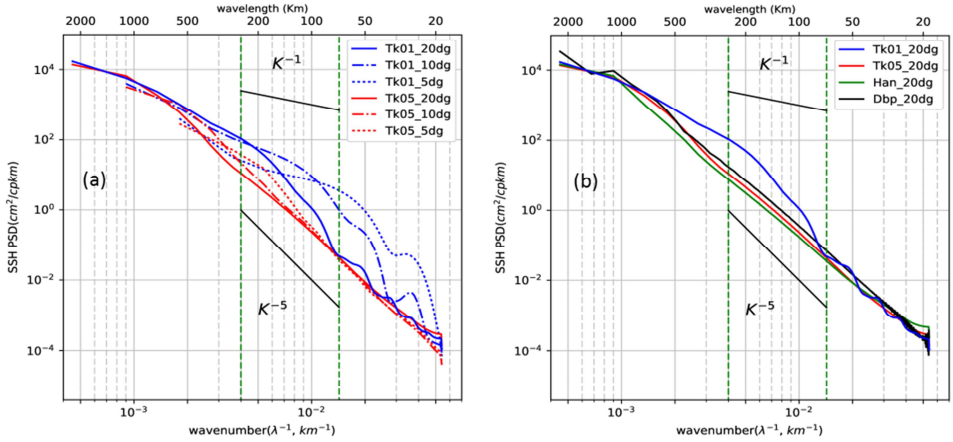

Figure 2: Sensitivity experiments for different spectral processing techniques applied to meridional SSH wavenumber spectra representative of the equatorial region. a) SSH wavenumber spectra using a Tukey 0.1 window (blue) and a Tukey 0.5 window (red) depending on segment lengths: 5° (dots), 10° (dash), 20° (line). b) SSH wavenumber spectra using different windowing over a 20° segment length: Tukey 0.1 window (Tk01, blue), Tukey 0.5 window (Tk05, red), Hanning window (Han, green). The double periodic method (Dbp, black) is also tested. For reference k^{-1} and k^{-5} curves are plotted. Units : cm^2/cpkm

Ocean Sci. Discuss., https://doi.org/10.5194/os-2018-49
Manuscript under review for journal Ocean Sci.
Discussion started: 28 June 2018
© Author(s) 2018. CC BY 4.0 License.

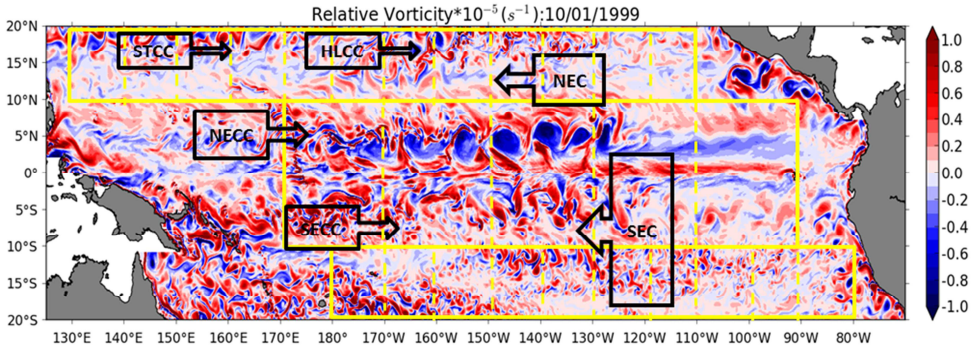

Figure 3: Snapshot of relative vorticity of the 1/12° G12d5 simulation. unit in 1.E5 s^{-1}. The yellow lines delineate the equatorial and off-equatorial regions. The dashed lines delineate square boxes for the different regions to compute wavenumber spectra. The black arrows illustrate the main zonal tropical currents (SEC: South Equatorial Current, SECC: South Equatorial CounterCurrent, NECC: North Equatorial CounterCurrent, NEC: North Equatorial Current, STCC: SubTropical CounterCurrent, HLCC: Hawaiin Lee Counter Current).

Ocean Sci. Discuss., https://doi.org/10.5194/os-2018-49
Manuscript under review for journal Ocean Sci.
Discussion started: 28 June 2018
© Author(s) 2018. CC BY 4.0 License.

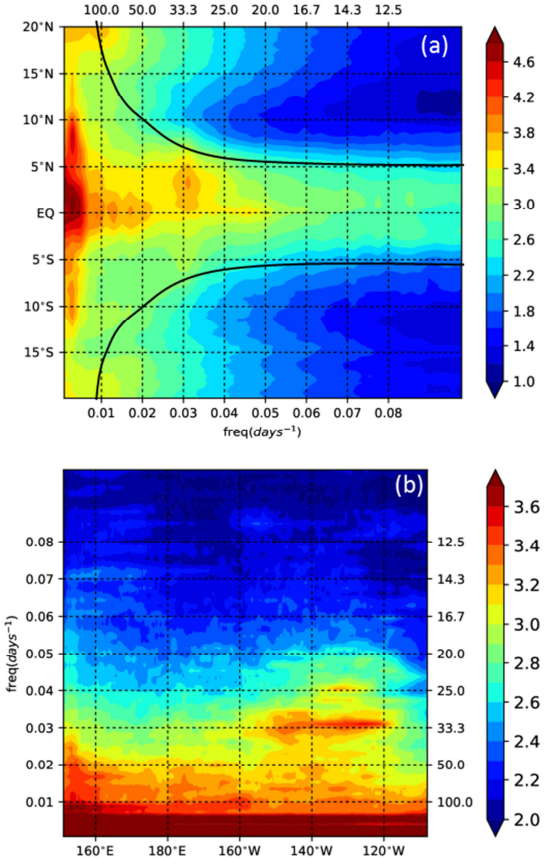

Figure 4: a) latitudinal distribution of the EKE Frequency power spectra computed at each model grid point of the G12d5 simulation, and averaged in longitude. The black line is the critical period from Lin et al. (2008). b) longitudinal distribution of the EKE Frequency power spectra computed at each model grid point of the G12d5 simulation, and averaged between 20°S-20°N. Units are in $\log_{10}$ of $cm^2/s^2/cpday$.

Ocean Sci. Discuss., https://doi.org/10.5194/os-2018-49
Manuscript under review for journal Ocean Sci.
Discussion started: 28 June 2018
© Author(s) 2018. CC BY 4.0 License.

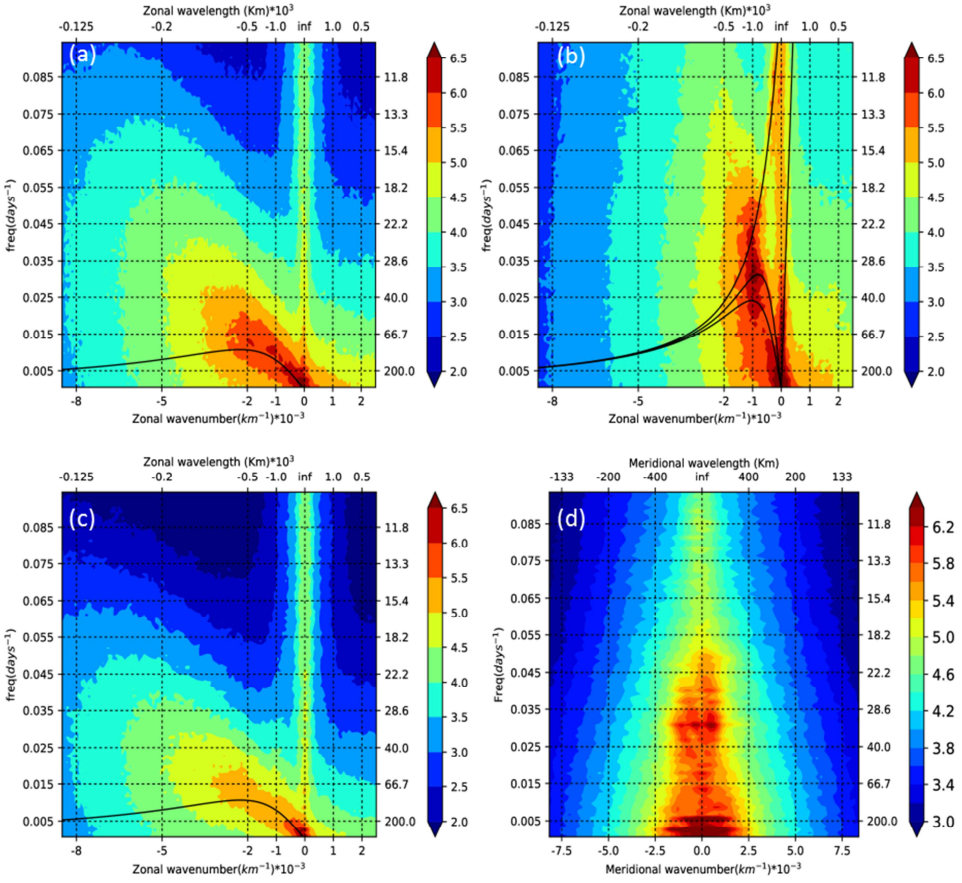

Figure 5: Zonal wavenumber-frequency EKE spectra averaged over a) 10°N-20°N region, b) 10°S-10°N region, and c) 10°S-20°S region. d) Meridional wavenumber-frequency EKE spectra covering 20°S-20°N averaged over the 120°W-150°W region. Superimposed on a) and c) are the theoretical dispersion curves for the first mode baroclinic waves. Superimposed on b) are the theoretical dispersion curves for the first 3 baroclinic wave modes, and the Kelvin wave mode. Units are in $\log_{10}$ of cm^2/s^2/cpday/cpkm.

Ocean Sci. Discuss., https://doi.org/10.5194/os-2018-49
Manuscript under review for journal Ocean Sci.
Discussion started: 28 June 2018
© Author(s) 2018. CC BY 4.0 License.

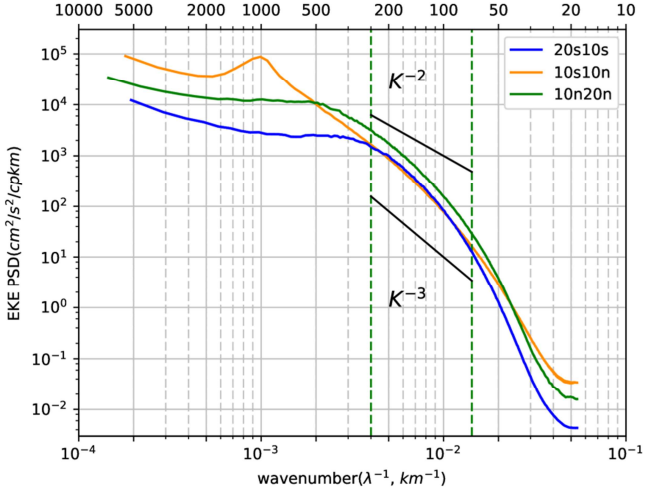

Figure 6: Zonal wavenumber EKE spectra averaged over the equatorial (orange line), and off-equatorial latitude bands (north: green; south: blue). Units are in cm^2/s^2/cpkm.

Ocean Sci. Discuss., https://doi.org/10.5194/os-2018-49
Manuscript under review for journal Ocean Sci.
Discussion started: 28 June 2018
© Author(s) 2018. CC BY 4.0 License.

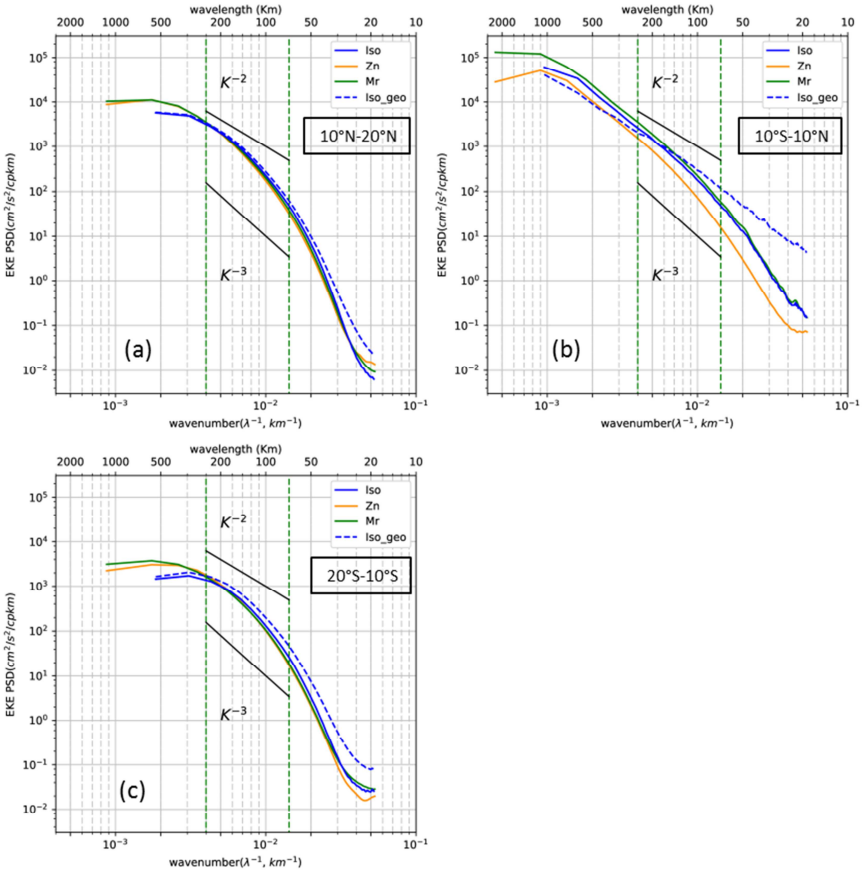

Figure 7: 1D zonal (orange), meridional (green); and 2D isotropic (blue) EKE wavenumber spectra averaged over a) 10°N-20°N, b) 10°S-10°N, and c) 10°S-20°S regions. The isotropic geostrophic EKE wavenumber spectra is also shown (EKEg, blue dash line). The vertical green dash lines delineate the fixed 70-250 km mesoscale range. For reference, k^{-2} and k^{-3} curves are plotted (black lines). Units are in cm^2/s^2/cpkm.

Ocean Sci. Discuss., https://doi.org/10.5194/os-2018-49
Manuscript under review for journal Ocean Sci.
Discussion started: 28 June 2018
© Author(s) 2018. CC BY 4.0 License.

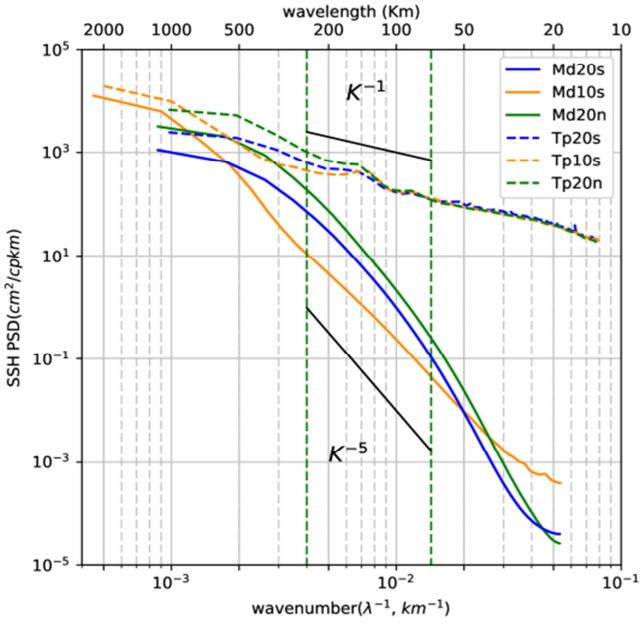

Figure 8: Meridional SSH wavenumber spectra averaged over the equatorial (orange), and off-equatorial latitude bands (north: green, south:blue) for the G12d5 simulation (line). Topex-Poseidon along track altimetric SSH wavenumber spectra are averaged over the same latitude bands (dash). Units are in cm^2/cpkm.

Ocean Sci. Discuss., https://doi.org/10.5194/os-2018-49
Manuscript under review for journal Ocean Sci.
Discussion started: 28 June 2018
© Author(s) 2018. CC BY 4.0 License.

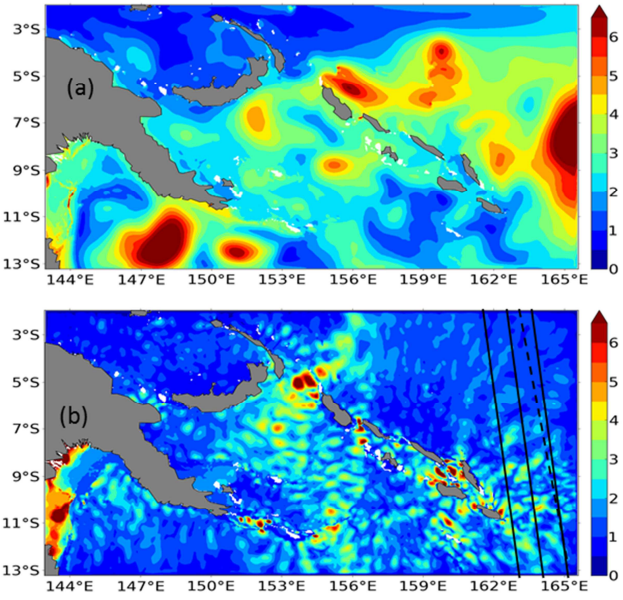

Figure 9: SSH variability of the 1/36° regional model with explicit tides (R36Th) over the 3 month simulation for a) the mesoscale signal, and b) the internal waves and internal tides defined by a 48 hr cutoff period. Units in cm^2. The SARAL/AltiKA (black line) and Jason-2 (dash line) tracks used to compute the altimetric spectra in Fig. 10 are superimposed.

Ocean Sci. Discuss., https://doi.org/10.5194/os-2018-49
Manuscript under review for journal Ocean Sci.
Discussion started: 28 June 2018
© Author(s) 2018. CC BY 4.0 License.

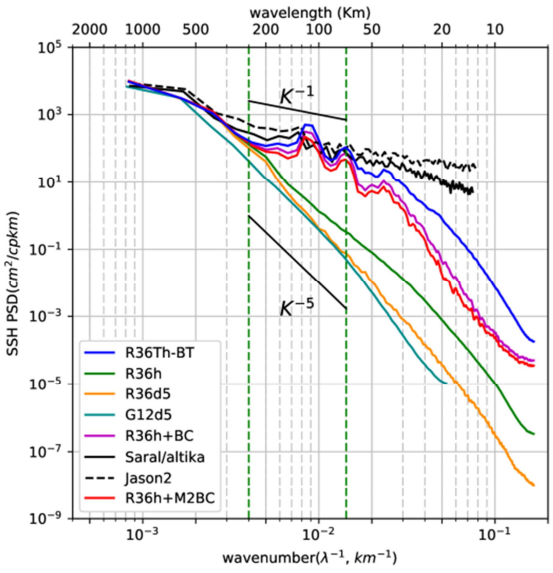

Figure 10: Meridional SSH wavenumber spectra averaged over 163°E-165°E for the hourly outputs of the 1/36° resolution regional model without tides (R36h, green), and 5 day averaged outputs (R36d5, orange). Meridional SSH spectra of the G12d5 simulation is in cyan. SSH meridional wavenumber spectra for the hourly outputs of the 1/36° regional model with explicit tides once the barotropic tides has been removed (R36Th-BT, in blue). The spectrum of the coherent baroclinic tides has been added to the spectrum of the model without tides (R36h+BC, purple), the contribution of the only M2 coherent baroclinic tide is in red (R36h+M2BC). The difference between the blue and purple curves corresponds with the incoherent internal tides. The corresponding along track SSH altimetric spectra for SARAL/AltiKa (line) and Jason-2 (dash) are in black. Units are in cm^2/cpkm.